Geophys. J. Int. (1990) **101**, 1–35

S–P conversion from the transition zone beneath Tonga and the nature of the 670 km discontinuity

Mark. A. Richards[1,2]* and Charles W. Wicks, Jr[2]*

[1]*Research School of Earth Sciences, Australian National University, Canberra,* ACT 2601, *Australia*
[2]*Department of Geological Sciences, University of Oregon, Eugene,* OR 97403, *USA*

Accepted 1989 June 19. Received 1989 May 10; in original form 1988 September 22

SUMMARY

Using more than 300 recordings of deep Tonga earthquakes from the Warramunga Seismic Array (central Australia), we have searched for short-period S–P conversions from the 670 km discontinuity arriving in the P-wave codas. The array seismograms were stacked and plotted in sections to optimize observation of $S_{670}P$ yielding the following results: For the northern part of Tonga (17.3°–18.4°S), $S_{670}P$-phases are observed with apparent conversion depths between about 660 and 680 km. For the central part (20.2°–22.3°S), $S_{670}P$ is not clearly observed. For the southern part (23.1°–25.7°S), $S_{670}P$ is observed for conversion depths between about 660 and 700 km. Intermittent occurrence of S–P conversion may result from different characteristic source radiation patterns among the three sections. Overall uncertainties in conversion depths (resulting from unmodelled lateral velocity variations and hypocentral location errors) are perhaps a few tens of kilometres. The S–P rays must travel either within or very close to the subducted slab because of the source/receiver/slab-dip geometry, so we conclude that large (>50 km) deformations of the 670 km discontinuity do not occur beneath Tonga. Our observations appear to be inconsistent with a chemical discontinuity at 670 km, but are easily explained if the 670 km discontinuity is a strongly pressure-dependent and, perhaps, moderately endothermic phase change in both the slab and surrounding mantle.

Key words: deep earthquakes, S–P conversion, discontinuity, Tonga subduction zone

1 INTRODUCTION

Short-period S–P conversions from the 670 km seismic discontinuity have been identified in P-wave codas from deep western Pacific earthquakes recorded by the Waramunga Seismic Array (WRA) in central Australia (Figs 1 and 2). For earthquakes beneath the Izu-Bonin Island arc, Barley (1977) and Barley *et al.* (1982) detected a P-coda phase, following P by about 20–30 s, which is not predicted by smooth seismic velocity *vs*. depth models. They labelled this phase X, and identified it as S–P conversion or scattering at about 650 km depth. Subsequently, Bock & Ha (1984) observed similar X-phases from events beneath the Tonga Island arc, inferring a conversion depth of about 700 km. Bock & Ha further concluded that such efficient short-period (~1 s) mode conversion requires an abrupt seismic discontinuity spanning less than about a 5 km depth interval.

If these S–P conversions have been correctly identified, their observation provides unique constraints on the fundamental nature and dynamical significance of the 670 km discontinuity. For example, the larger conversion depth (~700 km) found by Bock & Ha (1984) may result from dynamical or thermal deformation of the 670 km discontinuity beneath the Tonga slab. Because the origin of this seismic discontinuity is one of the most important (and contentious) issues in mantle dynamics, we have undertaken an extensive study involving a much larger data set than used by previous workers. Our results are roughly consistent with Barley *et al.* (1982) and Bock & Ha (1984): we find strong evidence for a sharp seismic discontinuity at approximately 660–690 km beneath the North and South sections of the Tonga subduction zone, implying only modest downward deformation of the discontinuity.

---

* Both authors now at: Department of Geology and Geophysics, University of California, Berkeley, CA 94720, USA.

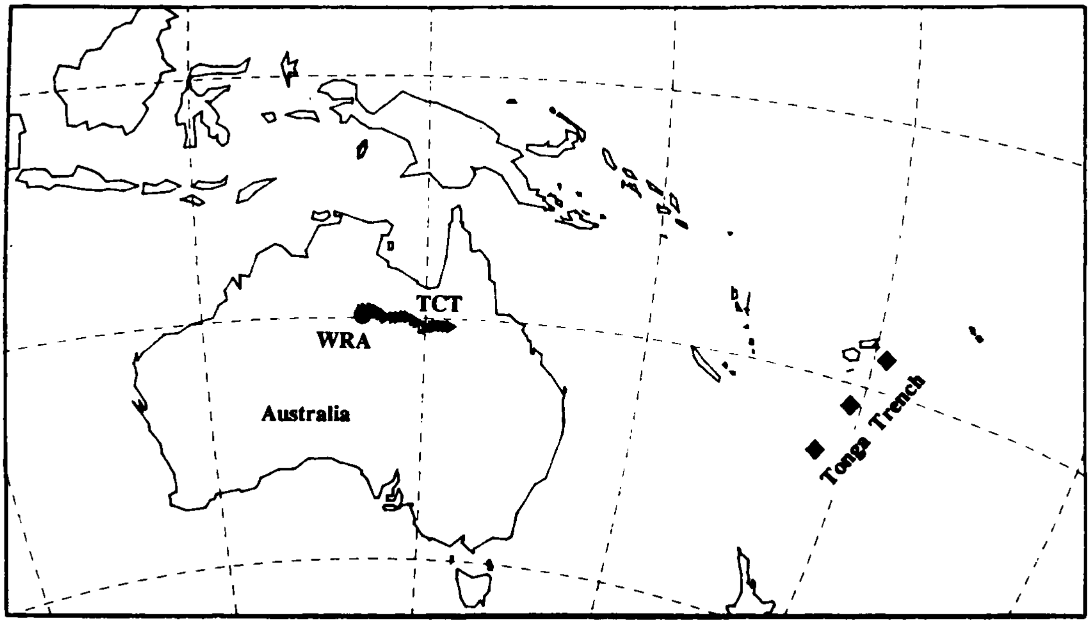

Figure 1. Regional map showing locations of the Warramunga Seismic Array (WRA) in central Australia (solid symbol) and the temporary TCT array stations (open triangles). The geographical centres of the North, Central, and South sections of deep Tonga earthquakes used in this study are shown by solid diamond symbols.

Although many kinds of geophysical and geochemical evidence have been brought to bear on the issue, it is not clear whether the 670 km discontinuity is the consequence of a phase change, a chemical boundary, or perhaps both. In particular, much ambiguity results from the fact that the seismological characteristics of the transition zone are not precisely known. The early semimic earth models of Jeffreys and Gutenberg included a rapid increase in seismic velocity and density in the depth range of 600–800 km, and subsequent observations of underside $P'_{670}P'$ reflections (Engdahl & Flinn 1969; Whitcomb & Anderson 1970; Richards 1972) imply a sharp discontinuity at about 670 km. Clearly (1981) and Muirhead (1985) have argued that these precursors to $P'P'$ could also be scattered $P3KP$-phases. However, Nakanishi (1986) has demonstrated by seismic array analysis that similar phases observed in Japan have the correct slowness for $P'_{670}P'$ and not for $P3KP$. Models derived from long-period body waves (e.g., Grand & Helmberger 1984) generally have a velocity contrast of 5–10 per cent at the 670 km level, but the depth extent and size of the velocity jump are not well-resolved. Nor, for that matter, is the true depth of the discontinuity, and various estimates fall in the range from 650 to 680 km. Here we arbitrarily use the designation '670 km' for convenience.

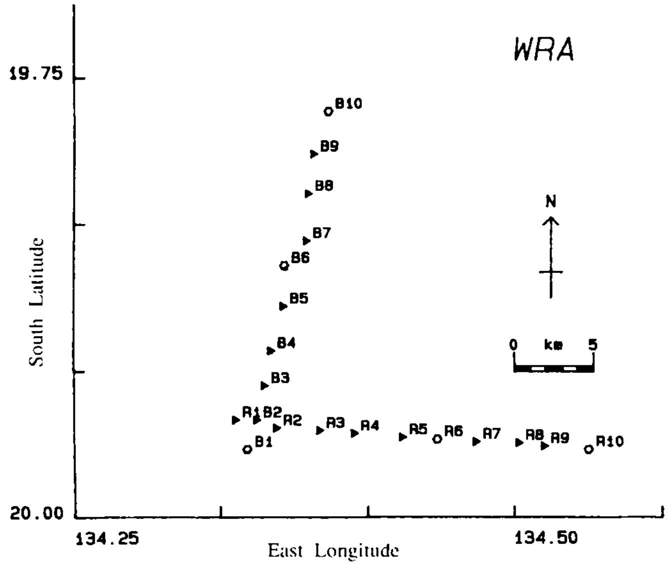

Figure 2. Map of the individual WRA seismometers. Solid symbols are vertical component only, and open symbols record three-component motion.

Observations of converted phases may provide more direct information. Faber & Muller (1984) studied long-period P–S and S–P conversions from the mantle transition zone, and found S–P precursors to S resulting from the 400 km and 670 km discontinuities. More recently, Paulssen (1985; 1987) has observed short-period P–S phases beneath European stations, concluding that there must be a sharp (<3 km thick) discontinuity at about 670 km depth. Paulssen (1985) also finds ~20 km variability in the depth of the discontinuity on relatively small (~200 km) length scales. Along with the studies of Barley *et al.* (1982) and Bock & Ha (1984), this constitutes fairly convincing evidence for a sharp 650–670 km discontinuity, at least in the regions sampled.

Unfortunately, it is not clear from high pressure experimental work on mantle minerals whether or not a major phase transition (spinel–perovskite) can cause such an abrupt change in density and seismic velocity. Jeanloz & Thompson (1983) argued that the phase change occurs over a depth interval of ~50 km, while Takahashi & Ito (1988) have recently concluded that the transition may occur much more rapidly. At present, neither a phase change nor a chemical boundary may be ruled out. However, these two alternatives imply very different regimes for mantle convection and for the dynamics of subducted slabs.

If the 670 km discontinuity is a chemical boundary layer which blocks penetration of slabs into the lower mantle, then very large deformations (of order ~100 km or more) of the discontinuity are expected below deeply subducting slabs (e.g., Hager & Raefsky 1981; Christensen & Yuen 1984; Kincaid & Olson 1987). On the other hand, elevation or depression (depending on the Clapeyron slope) of a phase boundary resulting from the presence of a cold slab might be less pronounced and more localized. Determining the true depth or morphology of the 670 km discontinuity beneath subduction zones could, therefore, provide a key constraint on the nature of the discontinuity. The *S–P* conversions from Tonga discovered by Bock & Ha (1984) offer the opportunity to directly measure deformation of the 670 km discontinuity beneath a subducting slab. As illustrated in Fig. 3, the *S–P* conversions must occur either within or very close to the subducted slab itself for $S_{670}P$ raypaths from Tonga to the WRA observatory. Consequently, data from Tonga should indicate the maximum deflection of the 670 km discontinuity.

In the previous work on *S–P* conversion beneath subduction zones, the main limitation was the fairly small number of observations. Barley *et al.* (1982) found only five $S_{670}P$ phases out of 21 earthquake records from the Izu-Bonin arc, and Bock & Ha (1984) found $S_{670}P$ for only 16 of 43 earthquakes beneath Tonga. (Possible reasons for the infrequent occurrence of $S_{670}P$ are discussed later.) Here we offer three significant improvements over these studies: (1) We have examined an order of magnitude more earthquake recordings (>300 events) from Tonga. (2) We have treated the three distinct sections (North, Central, and South) of the Tonga subduction zone separately; this allows us to detect regional variations. (3) The larger data set allows us to search more systematically for the $S_{670}P$-phase by stacking the entire data set.

The emphasis in this paper is mainly on the observation of $S_{670}P$, because its appearance on the WRA records from Tonga is unambiguous. There are a number of problems with precise interpretation, e.g., those associated with source radiation patterns, lateral velocity heterogeneity near the subducting slab, and $S_{670}P$ signal duration and amplitude. These issues are not treated in great detail here, because they are unlikely to strongly affect the basic results.

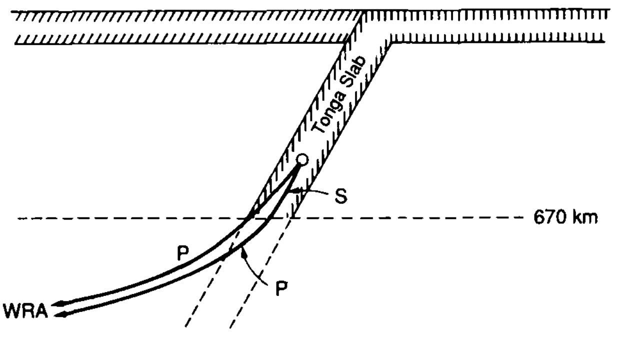

Figure 3. Idealized diagram for raypaths from the Tonga subduction zone to WRA. Both vertical and horizontal distances are to scale for a slab dipping 60° toward WRA and lithospheric thickness of 100 km. Takeoff angles for both *P* and *S–P* rays are approximately correct as shown.

2 EARTHQUAKE DATA

A large fraction of the world's deep earthquakes occur beneath the Tonga subduction zone. Those of magnitude $m_b > 4.5$ usually trigger the Warramunga Seismic Array. The first 7–15 min of each event are normally recorded, depending on whether or not the *S*-wave is strong enough to retrigger the array. The previous studies by Barley *et al.* (1982) and Bock & Ha (1984) included mostly data recorded on the old analogue recording system, and data processing was tedious. However, in 1978 WRA began digitally recording its 20 short-period (~1 s) vertical and 10 horizontal component channels. This has allowed us to process a very large number of events. More than 500 deep Tonga earthquakes of magnitude $m_b \geqslant 4.8$ have been recorded digitally at WRA. This is a remarkable data set and, as will become apparent later, gives us the capability of studying in detail many other interesting phases besides $S_{670}P$.

The distribution of deep seismicity is shown in the map view of Fig. 4(a) and the north–south cross-section of Fig. 5(a). There are three main clusters of hypocentres which Giardini & Woodhouse (1984) referred to as the North, Central, and South sections. A gap corresponding to the Louisville Ridge separates the Central and South sections, and the North section contains the very dense cluster often called the 'hook' region. Giardini & Woodhouse (1984, 1986) showed that these three sections are distinct seismically and tectonically, with clear differences in slab-dip and stress release patterns.

Since most of the earthquakes occur within these three clusters, we have restricted our attention to the events shown in Figs 4(b) and 5(b). Earthquakes that clearly generate the $S_{670}P$-phase are marked with an '×'. The hypocentres plotted are the ones actually used and include more than 100 events within each section. We chose the section boundaries to maximize the number of events while minimizing the length of slab or trench in each section. This allows us to concentrate on narrow sections of the subduction zone while maintaining a high density of data. As we show later, there are important differences in observations of $S_{670}P$ among the three sections.

The earthquake source parameters are given in Tables 1 to 3. For most events we have used the published locations of the International Seismic Centre (ISC). For some events between 1984 and 1986, locations are from the Preliminary Determination of Epicenters listing of the National Earthquake Information Service (NEIS). The ISC locations are generally in good agreement with other more careful determinations (e.g., Giardini & Woodhouse 1984; Bock 1987), probably because the station on Fiji provides good depth control. The potentially important effects of errors in depth determination are discussed later.

3 CHARACTERISTICS OF $S_{670}P$

The advantages of using deep earthquakes to observe $S_{670}P$ are twofold: (1) The *P*-waves from deep events are usually impulsive and followed by very quiet codas, because there is little near-surface scattering. This is crucial since $S_{670}P$ is a low-amplitude phase arriving within about 30 s of P. (2) The delay between $S_{670}P$ and P depends systematically upon the focal depth. This delay is the travel time difference between P and S waves travelling from the hypocentre to the 670 km discontinuity: deeper events give smaller delays. If the focal depth is well-determined, the $S_{670}P-P$ delay is diagnostic of the depth of $S_{670}P$ conversion.

The focal depth dependence of the $S_{670}P-P$ delay is shown in Fig. 6 (similar to Fig. 6 of Bock & Ha 1984). The light lines are theoretical delays calculated from PEMC (Dziewonski *et al.* 1975) for mantle velocity discontinuities at 650, 670, and 700 km depth. Measured delay times from Barley *et al.* (1982) and Bock & Ha (1984) are given by open symbols and ×, respectively. Bock & Ha's delays from Tonga cluster around theoretical curves for $S-P$ conversion depths of about 700–720 km, while Barley *et al.* from Izu-Bonin fall more consistently along the 650 km curve. The points plotted were selected from stacked event records for P-coda arrivals (with the correct slowness across the WRA array) which were judged to be abnormally large in amplitude. About two-thirds of the events previously examined were not selected as showing X-phase or $S_{670}P$-phase arrivals.

The strategy here is similar, but more objective. Instead of selecting events individually which appear to show an arrival at about the right time for $S_{670}P$ on the seismograms, we simply plot a section of stacked event records so that any consistent coda phases will stand out naturally (see, for example, Figs 10 and 11). This is very similar to finding reflection horizons in a seismic reflection section. Events that do not exhibit $S_{670}P$, while included in the section, simply do not contribute to the observed phase.

Our method is designed primarily to avoid picking spurious signals. Multiple focal activity or aftershocks

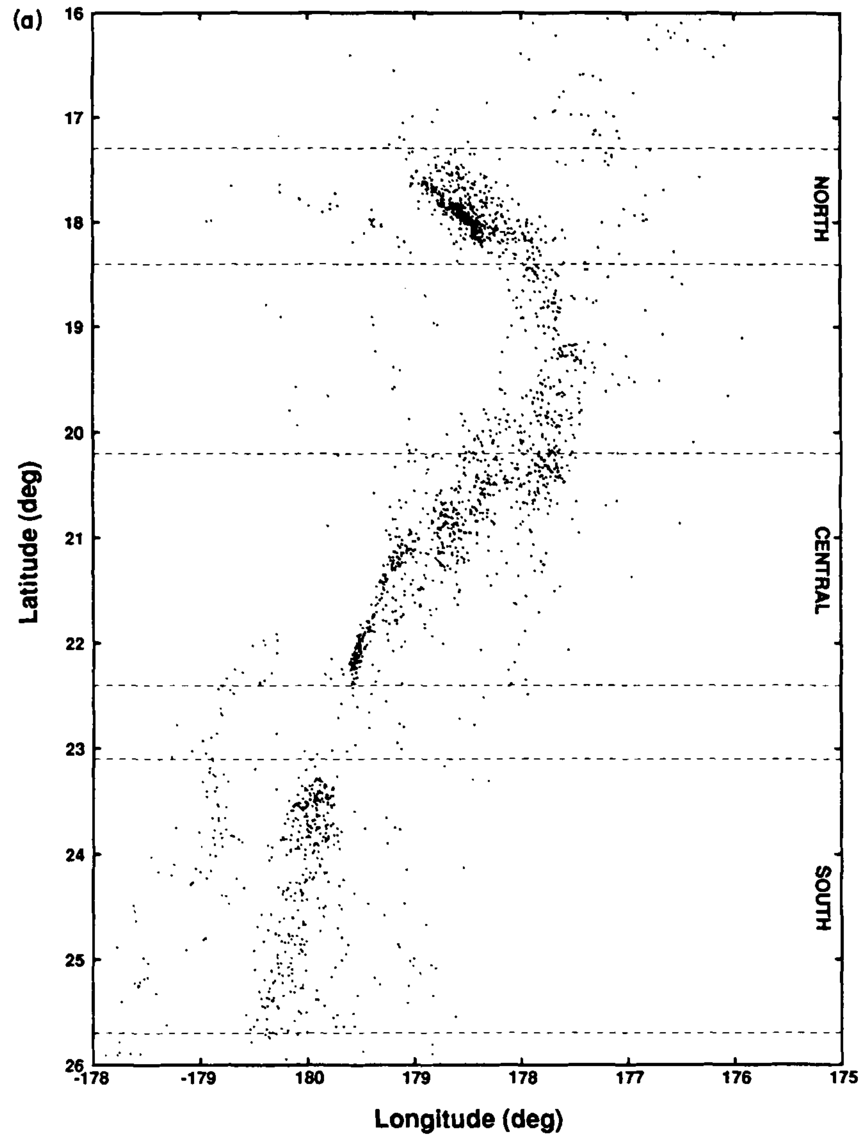

Figure 4. (a) Map view of hypocentres for deep Tonga earthquakes relocated by Giardini & Woodhouse (1984). (b) Map view of hypocentres for earthquakes used in this study. Locations are from the ISC and NEIS listings (see Tables 1–3). Events that exhibit strong $S_{670}P$ phases are shown by ×.

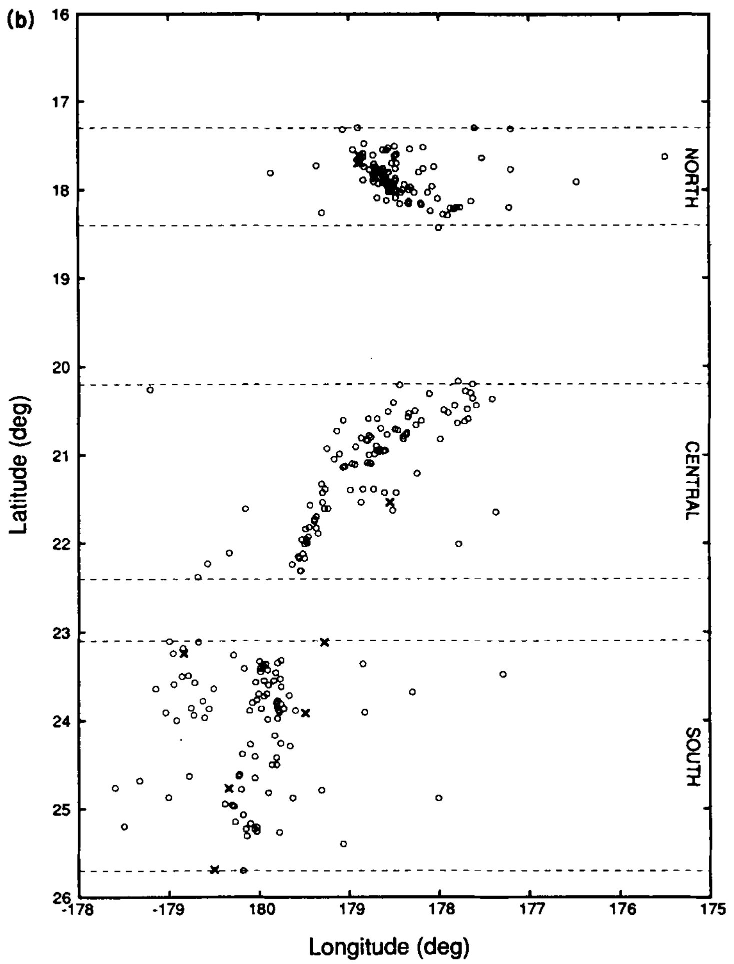

Figure 4. (*continued*)

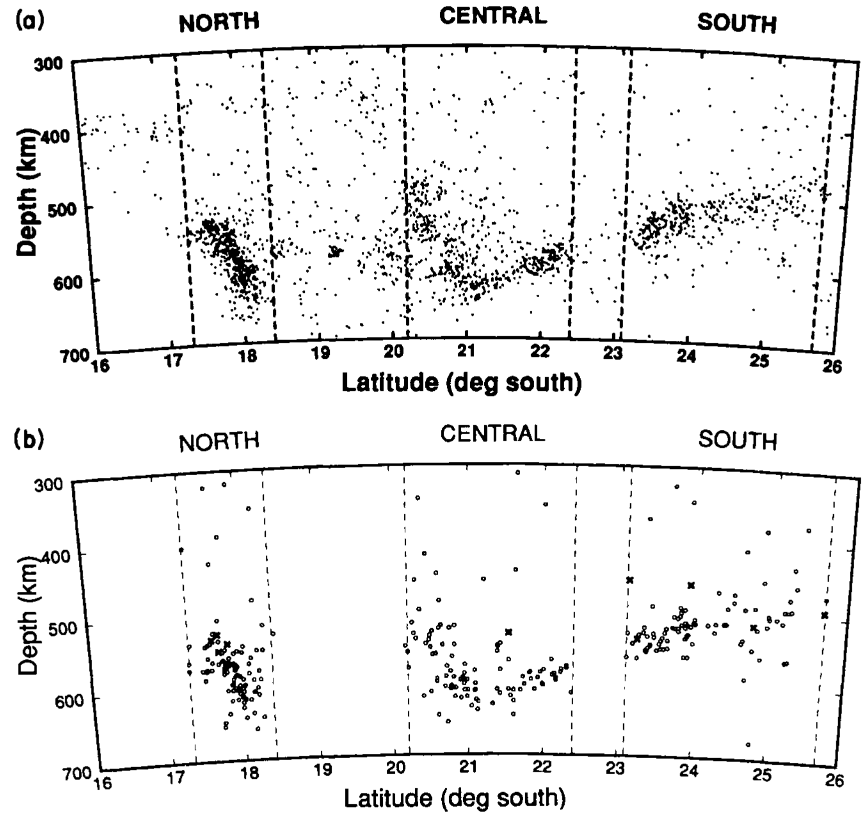

Figure 5. (a) North–south cross-section of hypocentres relocated by Giardini & Woodhouse (1984). (b) North–south cross-section of hypocentres used in this study. Events that exhibit strong $S_{670}P$ phases are shown by ×.

Table 1. North section event information.

Event Number	Data Source	Date *(yr mn dy)*			Time *(hr min sec)*			Latitude *(degree)*	Longitude *(degree)*	Magnitude *(m_b)*	Depth *(km)*
1	ISC	1978	6	28	14	31	55.1	17.93 S	178.53 W	4.9	571
2	ISC	1978	7	3	20	52	26.2	17.92 S	178.52 W	5.3	573
3	ISC	1978	11	11	6	42	14.4	17.73 S	179.36 W	5.0	653
4	ISC	1979	2	4	4	35	34.6	17.85 S	178.65 W	5.1	617
5	ISC	1979	2	11	8	46	41.1	17.75 S	178.70 W	5.1	561
6	ISC	1979	2	23	5	5	16.2	17.95 S	178.52 W	5.2	603
7	ISC	1979	2	25	9	28	40.3	17.91 S	178.56 W	4.9	583
8	ISC	1979	2	27	18	51	37.6	17.93 S	178.59 W	5.2	582
9	ISC	1979	4	12	0	14	20.7	18.03 S	178.12 W	5.4	616
10	ISC	1979	4	20	8	27	54.0	18.09 S	178.48 W	4.9	580
11	ISC	1979	6	29	14	11	22.9	17.92 S	178.62 W	5.3	568
12	ISC	1979	7	24	9	21	58.0	17.59 S	178.84 W	5.3	538
13	ISC	1979	7	28	4	56	16.5	18.16 S	178.43 W	5.0	606
14	ISC	1979	7	29	16	32	5.0	17.70 S	178.52 W	5.3	535
15	ISC	1979	8	23	0	25	42.9	17.86 S	178.72 W	5.3	567
16	ISC	1979	8	29	21	29	41.5	17.61 S	178.89 W	5.3	533
17	ISC	1979	9	20	22	9	13.0	17.30 S	177.60 W	5.1	564
18	ISC	1979	9	20	22	59	5.3	17.94 S	178.38 W	5.1	549
19	ISC	1979	9	21	1	12	32.5	17.77 S	177.20 W	5.0	390
20	ISC	1979	11	9	14	38	21.5	17.75 S	178.72 W	5.4	550
21	ISC	1979	12	3	4	0	40.1	18.01 S	178.47 W	5.2	605
22	ISC	1979	12	26	7	53	40.5	18.13 S	177.64 W	4.8	635
23	ISC	1980	1	4	4	39	2.7	17.91 S	178.72 W	5.2	571
24	ISC	1980	2	15	9	55	53.0	18.00 S	178.54 W	5.2	551
25	ISC	1980	2	24	16	33	32.0	17.95 S	178.57 W	5.1	583
26	ISC	1980	2	24	23	13	19.0	18.00 S	178.33 W	5.0	601
27	ISC	1980	2	25	2	45	26.0	18.20 S	177.80 W	5.0	600
28	ISC	1980	2	25	19	34	13.5	17.70 S	178.47 W	5.4	506
29	ISC	1980	3	2	2	34	39.0	18.03 S	178.42 W	5.0	615
30	ISC	1980	3	6	13	46	12.3	18.22 S	177.83 W	5.2	577
31	ISC	1980	4	22	6	55	28.9	18.24 S	178.09 W	5.5	589
32	ISC	1980	5	4	12	25	2.2	18.10 S	178.01 W	5.1	616
33	ISC	1980	6	14	19	32	35.8	18.28 S	177.95 W	5.5	549
34	ISC	1980	5	25	18	39	2.6	17.97 S	178.31 W	5.0	584
35	ISC	1980	5	31	11	24	8.6	18.15 S	178.34 W	4.9	606
36	ISC	1980	6	17	11	55	7.7	17.86 S	178.59 W	5.1	595
37	ISC	1980	6	26	0	46	26.2	17.80 S	178.56 W	5.3	577
38	ISC	1980	7	20	21	20	3.6	17.88 S	178.61 W	6.0	588
39	ISC	1980	8	18	8	8	0.8	17.87 S	178.48 W	5.0	594
40	ISC	1980	9	29	12	20	32.6	17.78 S	178.64 W	5.1	547
41	ISC	1980	12	4	18	58	54.1	17.81 S	179.87 W	5.1	635
42	ISC	1980	12	31	14	0	45.1	17.79 S	178.70 W	5.2	565
43	ISC	1981	1	8	18	56	19.2	18.12 S	178.58 W	5.0	559
44	ISC	1981	1	28	10	16	3.6	17.90 S	178.59 W	5.0	575
45	ISC	1981	2	19	10	31	33.0	18.03 S	178.27 W	4.8	641
46	ISC	1981	3	18	6	44	39.7	17.63 S	178.84 W	5.0	524
47	ISC	1981	4	21	15	27	23.6	17.80 S	178.64 W	5.2	570
48	ISC	1981	4	23	17	25	44.3	18.20 S	177.76 W	5.0	549
49	ISC	1981	6	12	9	9	47.2	17.54 S	178.32 W	5.0	574
50	ISC	1981	6	28	16	31	24.9	17.60 S	178.47 W	4.6	574
51	ISC	1981	7	26	4	52	0.7	17.70 S	178.90 W	5.0	549
52	ISC	1981	8	30	11	36	20.2	17.93 S	178.50 W	5.3	603
53	ISC	1981	9	17	12	42	25.5	18.20 S	177.22 W	5.2	353
54	ISC	1981	10	14	16	26	42.0	17.53 S	178.56 W	5.0	576
55	ISC	1981	10	20	13	51	45.7	18.26 S	179.30 W	5.5	641
56	ISC	1981	11	26	12	9	51.9	17.52 S	178.17 W	5.1	542
57	ISC	1982	1	1	10	53	7.2	18.01 S	178.49 W	5.4	588
58	ISC	1982	1	8	11	41	3.6	17.83 S	178.63 W	5.0	558
59	ISC	1982	1	17	10	54	22.2	17.74 S	178.83 W	5.0	562
60	ISC	1982	2	14	5	11	24.2	17.91 S	176.47 W	5.1	318
61	ISC	1982	4	22	16	17	11.4	18.02 S	178.52 W	5.0	597
62	ISC	1982	8	1	18	51	59.2	17.69 S	178.88 W	5.0	566
63	ISC	1982	12	15	10	17	22.3	18.16 S	178.33 W	4.9	657
64	ISC	1982	12	20	13	1	26.9	17.90 S	178.48 W	4.9	600

Table 1. (*continued*)

Event Number	Data Source	Date (*yr mn dy*)			Time (*hr min sec*)			Latitude (*degree*)	Longitude (*degree*)	Magnitude (m_b)	Depth (*km*)
65	ISC	1982	12	29	0	10	55.6	17.64 S	177.52 W	4.8	427
66	ISC	1983	1	8	8	10	34.2	17.96 S	178.07 W	5.0	596
67	ISC	1983	1	17	0	0	46.0	17.76 S	178.17 W	5.3	580
68	ISC	1983	10	4	20	35	20.0	18.00 S	178.40 W	5.1	620
69	ISC	1983	10	10	14	9	46.8	18.29 S	177.90 W	5.1	515
70	ISC	1983	11	23	5	48	33.5	18.13 S	178.33 W	5.6	606
71	ISC	1983	12	24	5	13	1.2	18.03 S	178.42 W	5.0	596
72	ISC	1984	1	8	7	30	53.3	18.21 S	177.87 W	5.1	610
73	ISC	1984	1	10	5	14	17.9	17.62 S	178.49 W	5.2	589
74	ISC	1984	1	20	3	53	3.4	17.82 S	178.60 W	5.3	539
75	ISC	1984	2	18	18	26	38.0	17.96 S	178.50 W	4.9	608
76	NEIS	1984	4	12	17	0	15.0	17.87 S	178.72 W	5.0	603
77	ISC	1984	4	25	4	19	30.8	17.31 S	177.20 W	5.6	404
78	ISC	1984	7	3	13	42	0.3	17.69 S	178.87 W	5.5	526
79	ISC	1984	7	3	13	47	5.3	17.71 S	178.72 W	5.1	527
80	ISC	1984	7	31	18	17	44.7	17.63 S	175.49 W	5.0	322
81	ISC	1984	9	1	21	16	13.0	18.17 S	178.19 W	5.3	480
82	NEIS	1984	11	15	10	15	7.7	17.32 S	179.07 W	5.2	539
83	ISC	1984	11	19	19	0	47.1	17.89 S	178.84 W	4.9	552
84	ISC	1984	11	22	17	7	36.3	17.74 S	178.05 W	5.8	647
85	ISC	1985	2	23	19	14	26.5	18.43 S	178.00 W	5.1	528
86	ISC	1985	4	6	19	47	44.6	17.93 S	178.67 W	5.3	616
87	ISC	1985	4	9	12	11	29.7	17.76 S	178.48 W	5.1	573
88	ISC	1985	5	16	1	6	18.7	17.76 S	178.62 W	5.2	576
89	ISC	1985	5	18	5	9	24.5	17.80 S	178.22 W	5.3	603
90	ISC	1985	6	17	1	9	26.8	17.55 S	178.62 W	4.9	558
91	ISC	1985	10	22	2	54	15.5	18.15 S	178.20 W	5.0	589
92	ISC	1985	11	16	23	30	10.9	17.61 S	178.73 W	5.0	564
93	NEIS	1985	11	4	14	47	21.0	17.51 S	178.49 W	5.0	588
94	NEIS	1986	3	2	4	8	38.9	18.00 S	178.53 W	5.0	627
95	ISC	1986	3	15	5	1	24.7	17.48 S	178.83 W	5.1	575
96	ISC	1986	4	1	10	13	41.3	18.02 S	178.56 W	5.7	543
97	ISC	1986	5	1	22	12	2.0	18.00 S	178.55 W	4.9	613
98	ISC	1986	5	31	12	45	54.0	17.30 S	178.90 W	5.1	574
99	ISC	1986	6	14	9	49	11.8	17.99 S	178.56 W	5.0	611
100	NEIS	1986	7	29	11	57	47.9	17.55 S	178.58 W	5.1	558
101	NEIS	1984	5	18	7	28	4.1	17.55 S	178.96 W	4.8	540
102	NEIS	1984	6	25	16	58	16.4	18.09 S	178.68 W	4.7	567
103	NEIS	1984	6	30	12	10	10.1	17.77 S	178.77 W	4.8	571

occuring within about 30 s of the main shock are probably the main source of such 'false alarms'. The $S_{670}P$-phase has almost the same slowness as P, so it is difficult to distinguish between aftershocks and $S_{670}P$ on an event-by-event basis using only the WRA recordings. Since the delay between main shock and aftershock should be random, this source of error is subdued by displaying a large number of events in section. As a preview, the heavy solid line in Fig. 6 gives our best fitting delay time curve determined from a section of events from North Tonga.

4 DATA PROCESSING AND RESULTS

The Warramunga Seismic Array is a typical L-shaped UKAEA array (Fig. 2). The two 20 km long arms are oriented roughly N–S and E–W, and each consists of ten 1-Hz vertical seismometers spaced about 2 km apart. Five of the stations also record 3-component motion. All data is recorded digitally at 20 samples per second. The facility is jointly operated by the United Kingdom Defence Ministry and the Australian National University.

Figure 7(a) (event number 15, Table 1) shows the first minute of all 20 vertical channels for an event (magnitude 5.3, depth 567 km) from North Tonga that exhibits the phase $S_{670}P$. Fig. 7(b) shows event number 45 (magnitude 4.8, depth 641 km) which has no strong coda phases. Stations B1–B10 are from south to north and stations R1–R10 are from west to east. Both of the events shown give impulsive P arrivals and little coda 'noise' beyond about 7 s after P. These recordings are typical of the more than 300 events used in this study. Two prominent arrivals follow P in Event A by about 12 s and 17 s. As we show later, the 12-s arrival can be identified as $S_{670}P$ after analysis of many earthquakes from the same part of Tonga.

4.1 Phased-array stacking

The power of a short-period array is the ability to stack and beam-form seismograms. Since the hypocentral locations of Tonga events with magnitude ⩾4.8 are generally well-determined by the ISC, the array can be tuned according to the correct azimuth and slowness of the P and $S_{670}P$ phases.

Figure 8(a) shows a simple linear stack of all 20 channels for event no. 15 using the known event azimuth and sweeping over slowness from 0.05 to 0.09 s km^{-1}. The two arrivals at 12 and 17 s after P are strongly enhanced by linear stacking. The correct slowness for both P and $S_{670}P$ is about 0.07 s km^{-1}, and this slowness does indeed maximize the amplitudes. However, the stacked phases are not very sensitive to the slowness, as shown by Fig. 8(a). Linear

Table 2. Central section event information.

Event Number	Data Source	Date *(yr mn dy)*			Time *(hr min sec)*			Latitude *(degree)*	Longitude *(degree)*	Magnitude *(m_b)*	Depth *(km)*
104	ISC	1978	8	17	8	32	19.4	22.17 S	179.56 W	5.5	597
105	ISC	1978	10	11	11	14	49.4	22.38 S	179.31 E	5.2	614
106	ISC	1978	12	2	4	15	49.8	20.20 S	177.63 W	5.1	558
107	ISC	1978	10	27	5	51	39.0	22.11 S	179.66 E	5.0	569
108	ISC	1978	10	27	6	24	57.2	20.95 S	178.60 W	5.3	602
109	ISC	1978	12	21	0	35	50.5	21.84 S	179.49 W	5.6	596
110	ISC	1979	1	4	9	25	48.8	21.54 S	178.55 W	5.1	533
111	ISC	1979	1	20	17	55	17.9	22.31 S	179.54 W	5.2	580
112	ISC	1979	2	10	8	27	57.4	20.41 S	178.51 W	5.0	619
113	ISC	1979	3	12	1	11	51.1	20.31 S	178.11 W	5.0	540
114	ISC	1979	7	8	8	55	46.9	22.15 S	179.57 W	5.4	588
115	ISC	1979	7	18	0	30	45.1	21.39 S	178.73 W	5.2	558
116	ISC	1979	7	20	1	10	28.9	20.53 S	178.34 W	5.2	562
117	ISC	1979	8	15	22	1	15.1	20.30 S	177.65 W	5.0	459
118	ISC	1979	8	18	23	42	48.8	22.12 S	179.52 W	5.2	590
119	ISC	1979	8	23	14	23	4.3	21.43 S	179.30 W	5.0	616
120	ISC	1979	10	2	19	18	12.8	20.59 S	178.69 W	5.0	595
121	ISC	1979	10	14	11	35	36.5	21.99 S	179.48 W	5.1	602
122	ISC	1979	10	23	1	38	14.7	20.93 S	179.25 W	5.3	594
123	ISC	1979	10	29	22	41	11.7	20.51 S	178.57 W	5.3	613
124	ISC	1979	11	6	1	25	0.6	21.09 S	178.80 W	5.6	584
125	ISC	1979	11	25	0	35	16.8	21.75 S	179.39 W	5.0	603
126	ISC	1979	11	25	11	38	1.4	22.01 S	179.50 W	5.4	583
127	ISC	1979	11	28	5	21	25.5	20.73 S	179.14 W	5.3	655
128	ISC	1979	12	8	20	4	54.4	20.84 S	178.80 W	4.9	608
129	ISC	1980	1	15	4	25	44.8	22.17 S	179.50 W	5.5	594
130	ISC	1980	1	30	11	29	29.0	21.73 S	179.39 W	5.4	593
131	ISC	1980	2	13	20	38	19.9	21.10 S	178.76 W	5.4	602
132	ISC	1980	2	18	17	17	13.9	21.43 S	178.48 W	5.4	583
133	ISC	1980	2	19	8	57	30.7	21.93 S	179.46 W	5.3	594
134	ISC	1980	2	22	10	48	39.7	21.61 S	179.84 E	5.2	645
135	ISC	1980	4	27	20	43	13.8	21.54 S	178.87 W	4.6	570
136	ISC	1980	4	30	11	25	33.3	20.26 S	178.79 E	4.9	518
137	ISC	1980	5	9	23	2	20.9	20.36 S	177.63 W	5.1	500
138	ISC	1980	6	17	8	42	56.9	20.21 S	178.44 W	5.5	580
139	ISC	1980	6	18	13	0	14.3	21.21 S	178.25 W	5.2	459
140	ISC	1980	8	13	4	20	38.9	21.40 S	178.99 W	4.8	551
141	ISC	1980	9	6	15	33	25.1	21.96 S	179.53 W	5.0	586
142	ISC	1980	9	16	23	33	40.8	20.59 S	178.79 W	5.2	599
143	ISC	1980	10	2	15	49	36.3	20.99 S	178.72 W	5.1	597
144	ISC	1980	10	3	1	53	16.5	20.17 S	177.79 W	5.4	550
145	ISC	1981	3	7	9	46	25.9	21.96 S	179.48 W	4.9	586
146	ISC	1981	2	5	21	46	38.1	20.44 S	177.83 W	5.2	547
147	ISC	1981	2	6	7	23	7.0	21.11 S	178.94 W	5.6	624
148	ISC	1981	3	31	10	48	11.4	21.00 S	178.78 W	5.1	611
149	ISC	1981	4	25	5	36	41.3	22.23 S	179.42 E	5.6	586
150	ISC	1981	6	13	4	25	45.8	20.52 S	177.90 W	5.1	530
151	ISC	1981	6	29	12	4	5.5	20.71 S	178.49 W	5.0	592
152	ISC	1981	7	10	23	5	43.2	21.33 S	179.31 W	5.0	630
153	ISC	1981	10	7	3	2	12.7	20.70 S	178.65 W	5.9	606
154	ISC	1981	10	7	18	22	23.2	20.77 S	178.58 W	4.5	609
155	ISC	1981	10	7	23	39	48.0	20.83 S	178.81 W	5.0	620
156	ISC	1981	11	13	6	7	4.1	20.62 S	177.72 W	5.3	488
157	ISC	1981	11	25	23	51	15.4	20.81 S	178.87 W	5.8	593
158	ISC	1981	12	2	15	15	37.0	21.82 S	179.45 W	5.5	587
159	ISC	1982	3	12	10	34	42.9	21.61 S	179.24 W	4.9	611
160	ISC	1982	4	7	13	57	27.2	20.57 S	178.35 W	4.9	561
161	ISC	1982	5	27	21	48	6.8	20.78 S	178.78 W	5.1	605
162	ISC	1982	5	28	6	35	44.1	20.80 S	178.76 W	5.2	608
163	ISC	1982	6	19	8	53	11.6	21.57 S	179.44 W	5.2	619
164	ISC	1982	6	19	18	49	2.6	21.09 S	178.77 W	4.9	612
165	ISC	1982	7	15	19	16	17.6	20.28 S	177.71 W	5.2	533
166	ISC	1982	7	16	14	33	41.1	21.39 S	178.85 W	5.3	550
167	ISC	1982	7	21	6	5	5.5	22.00 S	179.47 W	5.1	604

Table 2. (*continued*)

Event Number	Data Source	Date (*yr mn dy*)			Time (*hr min sec*)			Latitude (*degree*)	Longitude (*degree*)	Magnitude (m_b)	Depth (*km*)
168	ISC	1982	11	9	0	46	55.5	21.43 S	178.61 W	5.1	547
169	ISC	1983	11	30	2	16	43.3	20.49 S	177.95 W	5.2	536
170	ISC	1982	12	4	0	24	21.6	20.94 S	178.66 W	5.0	597
171	ISC	1983	1	2	22	9	6.1	20.96 S	178.62 W	5.1	611
172	ISC	1983	3	9	17	53	9.2	20.50 S	178.27 W	5.2	552
173	ISC	1983	2	11	17	40	54.3	20.59 S	177.68 W	5.1	450
174	ISC	1983	3	2	14	12	34.0	20.99 S	179.11 W	5.1	620
175	ISC	1983	4	6	18	8	7.1	21.61 S	179.28 W	5.1	626
176	ISC	1983	7	1	3	16	5.2	20.75 S	178.36 W	5.4	526
177	ISC	1983	9	15	15	56	13.2	20.90 S	178.70 W	4.9	597
178	ISC	1983	9	30	17	31	22.5	21.13 S	179.05 W	5.1	638
179	ISC	1984	1	11	9	2	27.0	20.96 S	178.66 W	5.2	576
180	ISC	1984	1	17	19	49	58.2	22.24 S	179.64 W	5.4	582
181	NEIS	1984	3	18	7	54	28.8	21.65 S	177.38 W	5.3	312
182	ISC	1984	4	4	5	30	59.1	21.39 S	179.27 W	5.1	610
183	ISC	1984	4	22	3	33	0.5	21.83 S	179.37 W	5.7	586
184	ISC	1984	9	15	10	59	42.3	20.77 S	178.37 W	5.2	585
185	ISC	1984	7	20	13	55	39.5	20.79 S	178.40 W	5.1	565
186	ISC	1984	9	25	3	7	12.2	22.31 S	179.55 W	5.1	577
187	ISC	1984	10	19	3	30	22.2	20.44 S	177.59 W	4.9	423
188	ISC	1984	10	20	21	22	11.3	20.72 S	178.46 W	5.3	578
189	ISC	1984	11	15	5	52	30.3	20.37 S	177.41 W	5.6	346
190	ISC	1984	11	16	3	54	12.8	21.54 S	179.30 W	5.1	610
191	ISC	1984	11	18	4	35	57.0	21.70 S	179.37 W	5.0	611
192	ISC	1984	12	27	3	26	6.8	21.89 S	179.35 W	5.2	610
193	ISC	1985	1	9	1	32	37.9	20.61 S	179.07 W	5.3	645
194	ISC	1985	1	13	21	20	1.3	20.64 S	177.80 W	5.0	522
195	ISC	1985	1	25	7	44	9.8	20.82 S	178.40 W	4.9	549
196	ISC	1985	2	4	6	12	31.9	20.66 S	178.26 W	4.6	549
197	ISC	1985	2	5	15	7	23.1	20.48 S	177.69 W	5.3	542
198	ISC	1985	3	10	5	9	10.9	21.05 S	179.17 W	5.5	633
199	ISC	1985	3	15	0	16	1.6	20.61 S	178.20 W	5.6	526
200	ISC	1985	8	24	6	53	15.7	22.01 S	177.79 W	5.5	355
201	ISC	1985	12	25	22	15	9.1	21.63 S	178.52 W	5.5	446
202	ISC	1985	11	27	4	18	4.0	21.10 S	178.97 W	5.3	611
203	ISC	1985	4	2	3	21	40.9	21.14 S	179.07 W	5.4	627
204	NEIS	1985	8	23	22	0	58.8	20.95 S	178.69 W	5.0	588
205	ISC	1985	9	8	22	46	5.6	20.91 S	178.93 W	5.2	622
206	ISC	1985	11	21	18	44	24.8	20.82 S	177.99 W	5.3	523

stacks for event no. 45 are shown in Fig. 8(b), showing no clear coda phases.

Alternatives to linear stacking have been developed to improve event detection capabilities with seismic arrays. The nonlinear '*n*th root' method (Muirhead 1968; Kanasewich *et al.* 1973) has been found to improve detection thresholds for atomic bomb tests and it also improves azimuth and slowness determinations for earthquakes. The method consists of taking the *n*th (usually 4th) root of each data point while preserving the sign before stacking, then raising the result for each time point after stacking back to the *n*th power. This nonlinear stacking method is particularly useful for enhancing coherent phases and suppressing non-Gaussian noise (Muirhead & Datt 1976). The most common type of non-Gaussian noise is a large electronic spike or data dropout on a single channel that can create a spurious signal that remains after linear stacking. The *n*th root method has been used extensively in processing WRA data, including the Bock & Ha (1984) study of $S_{670}P$.

We have obtained much better observations of $S_{670}P$ using the *n*th method instead of simple linear stacking. Fig. 9(a) shows nonlinear (4th root) stacks of event no. 15, again sweeping over slowness. The advantage of the *n*th root method for enhancing the coherent phases and suppressing noise is obvious in comparing Figs 8(a) and 9(a). Also, better slowness discrimination is obtained from nonlinear stacks as can be seen by comparing the effect of stacking slowness on the relative *P*-wave amplitudes in Figs 8 and 9. However, note the waveform distortion in Fig 9(a) which is the main disadvantage of nonlinear stacking. Waveforms are preserved only for very large signal-to-noise ratios (e.g., the *P* arrival). Fig. 9(b) shows the nonlinear stacks for event no. 45, and the contrasting lack of coherent *P*-coda phases is even more obvious than in Fig. 8(b).

4.2 Hypocentral depth sections: North Tonga

From the single-event analyses above it is impossible to determine the nature of the two coda phases of event no. 15. Since they have the same slowness as *P*, they could be results of multiple focal activity. Because the delay between $S_{670}P$ and *P* is almost entirely a function of hypocentral depth, this ambiguity can be resolved by plotting stacked records as a function of focal depth as in Fig. 10(a). In this section plot, all events are aligned on the time axis so that the maximum *P*-wave amplitude falls on time $t = 0$. Each trace is a linear stack for the first 170 s of a single event from North Tonga, stacked for the expected slowness and azimuth of $S_{670}P$ and normalized to its own maximum

Table 3. South section event information.

Event Number	Data Source	Date *(yr mn dy)*	Time *(hr min sec)*	Latitude *(degree)*	Longitude *(degree)*	Magnitude *(m_b)*	Depth *(km)*
207	ISC	1978 6 29	16 33 24.5	24.87 S	178.99 E	5.0	560
208	ISC	1978 9 23	16 11 32.6	23.36 S	179.93 W	5.0	556
209	ISC	1978 9 24	7 32 26.6	23.62 S	179.76 W	5.0	524
210	ISC	1978 12 24	9 43 37.2	23.32 S	179.76 W	4.8	530
211	ISC	1979 1 29	5 43 0.3	24.65 S	179.95 E	5.5	493
212	ISC	1979 2 9	23 12 17.7	24.61 S	179.78 E	5.0	540
213	ISC	1979 4 3	13 7 16.3	24.29 S	179.66 W	5.0	471
214	ISC	1979 7 3	2 50 18.8	23.92 S	179.49 W	5.0	462
215	ISC	1979 7 20	22 45 0.7	23.37 S	179.96 W	5.4	535
216	ISC	1979 9 10	7 38 41.4	25.70 S	179.82 E	5.2	472
217	ISC	1979 10 2	15 41 3.9	23.18 S	179.15 E	4.9	545
218	ISC	1979 11 12	7 34 16.6	24.41 S	179.95 E	5.1	515
219	ISC	1979 11 20	19 28 32.4	23.82 S	179.76 W	5.0	518
220	ISC	1979 11 24	6 10 40.1	24.68 S	178.67 E	5.1	589
221	ISC	1979 12 9	1 9 20.2	23.78 S	179.37 E	4.9	527
222	ISC	1980 1 6	22 10 49.6	23.80 S	179.81 W	5.0	506
223	ISC	1980 2 9	19 29 15.7	23.87 S	179.44 E	5.2	537
224	ISC	1980 4 15	4 10 22.9	24.63 S	179.77 E	4.9	412
225	ISC	1980 5 20	4 24 47.9	23.78 S	179.80 W	5.2	523
226	ISC	1980 6 13	23 21 42.0	23.43 S	179.91 W	5.0	493
227	ISC	1980 7 17	14 6 29.8	23.59 S	179.05 E	4.9	552
228	ISC	1980 8 31	9 51 22.0	24.00 S	179.08 E	5.0	516
229	ISC	1980 9 11	10 30 5.7	25.69 S	179.50 E	4.9	492
230	ISC	1980 9 15	21 21 32.8	24.17 S	179.83 W	5.0	517
231	ISC	1980 11 12	4 28 36.5	23.89 S	179.89 E	5.0	518
232	ISC	1980 12 5	7 14 18.6	24.76 S	178.40 E	5.3	549
233	ISC	1981 1 1	9 12 48.0	23.77 S	179.97 E	5.0	509
234	ISC	1981 2 8	0 5 20.8	23.73 S	179.95 W	5.3	523
235	ISC	1981 3 21	22 15 3.0	25.27 S	179.78 W	5.1	434
236	ISC	1981 4 5	10 27 9.8	25.07 S	179.82 E	5.2	505
237	ISC	1981 4 28	21 14 47.1	23.70 S	179.99 E	6.0	522
238	ISC	1981 5 3	12 49 7.2	24.88 S	179.63 W	5.0	454
239	ISC	1981 5 27	1 45 10.4	25.31 S	179.86 E	5.3	460
240	ISC	1981 5 31	22 26 10.3	23.12 S	179.28 W	4.6	458
241	ISC	1981 6 4	20 35 57.4	23.86 S	179.24 E	4.6	562
242	ISC	1981 6 27	2 15 32.6	25.20 S	178.50 E	5.0	563
243	ISC	1981 7 26	7 29 57.0	23.87 S	179.98 W	5.2	522
244	ISC	1981 8 2	0 49 45.1	23.45 S	179.99 W	5.1	531
245	ISC	1981 8 17	17 7 40.9	25.40 S	179.07 W	5.5	376
246	ISC	1981 9 11	8 33 41.8	23.24 S	179.16 E	5.1	539
247	ISC	1981 9 25	16 43 21.9	23.36 S	178.85 W	5.2	372
248	ISC	1981 10 18	15 17 16.4	24.77 S	179.66 E	4.9	516
249	ISC	1981 10 23	2 40 11.1	24.78 S	179.80 E	5.0	491
250	ISC	1981 10 24	4 57 53.0	24.88 S	178.01 W	5.1	383
251	ISC	1981 11 15	23 22 34.1	23.94 S	179.27 E	5.1	520
252	ISC	1981 11 22	13 47 40.3	23.86 S	179.80 W	5.4	497
253	ISC	1981 11 25	17 55 27.5	23.64 S	179.49 E	5.0	540
254	ISC	1981 12 22	20 59 46.2	24.82 S	179.90 W	4.9	521
255	ISC	1981 12 29	14 20 50.0	23.80 S	179.92 E	4.8	494
256	ISC	1982 2 7	8 53 48.8	23.11 S	179.32 E	4.9	531
257	ISC	1982 2 9	11 45 28.7	25.26 S	179.97 E	5.1	493
258	ISC	1982 2 13	23 24 37.5	23.57 S	179.28 E	4.9	537
259	ISC	1982 2 21	14 18 33.4	23.87 S	179.73 W	5.0	515
260	ISC	1982 3 3	8 6 46.0	23.91 S	178.83 W	4.3	347
261	ISC	1982 3 7	8 50 6.7	23.46 S	179.82 W	4.8	536
262	ISC	1982 5 1	22 11 26.9	23.91 S	178.96 E	5.1	562
263	ISC	1982 5 12	10 3 31.2	24.63 S	179.22 E	5.6	536
264	ISC	1982 5 14	18 29 37.2	23.97 S	179.39 E	5.0	543
265	ISC	1982 11 3	18 7 46.9	25.23 S	179.85 E	5.3	477
266	ISC	1982 12 19	7 38 10.1	23.55 S	179.95 W	4.7	541
267	ISC	1982 12 22	15 32 34.7	23.24 S	179.04 E	5.2	565
268	ISC	1982 12 24	0 29 35.3	23.33 S	180.00 W	4.5	523
269	ISC	1983 5 13	23 16 10.2	24.79 S	179.31 W	5.0	677
270	ISC	1983 6 26	17 9 2.5	23.49 S	179.21 E	4.9	532

Table 3. (*continued*)

Event Number	Data Source	Date (*yr mn dy*)			Time (*hr min sec*)			Latitude (*degree*)	Longitude (*degree*)	Magnitude (m_b)	Depth (*km*)
271	ISC	1983	6	27	14	10	4.5	23.89 S	179.79 W	5.3	533
272	ISC	1983	7	9	12	28	46.2	25.21 S	179.97 E	5.1	494
273	ISC	1983	9	16	8	9	27.1	23.98 S	179.80 W	6.0	515
274	ISC	1983	9	19	18	41	42.9	23.60 S	179.90 W	5.0	530
275	ISC	1983	10	24	17	37	43.1	23.38 S	179.96 W	5.2	551
276	ISC	1983	11	8	17	52	26.0	23.53 S	179.77 W	5.1	545
277	ISC	1983	11	26	13	35	49.5	24.27 S	179.90 E	5.0	515
278	ISC	1984	1	19	16	15	15.6	23.68 S	178.30 W	5.8	326
279	ISC	1984	3	12	10	50	48.9	23.41 S	179.99 W	5.5	546
280	ISC	1984	7	18	6	1	54.1	23.89 S	179.60 W	4.9	534
281	ISC	1984	9	6	7	24	31.0	23.35 S	179.80 W	5.0	554
282	ISC	1984	9	20	12	44	25.3	24.42 S	179.81 W	5.2	493
283	ISC	1984	9	26	11	33	46.8	23.99 S	179.91 W	5.2	510
284	ISC	1984	10	24	2	28	59.0	24.50 S	179.81 W	5.0	473
285	ISC	1984	10	30	15	12	30.1	24.50 S	179.86 W	4.9	484
286	ISC	1984	11	12	10	51	45.7	24.96 S	179.70 E	5.1	501
287	NEIS	1984	11	12	12	4	56.9	25.23 S	179.95 E	5.0	562
288	NEIS	1984	11	22	16	10	13.2	23.10 S	179.00 E	5.1	564
289	ISC	1984	11	24	17	17	43.9	23.26 S	179.71 E	5.0	533
290	ISC	1984	11	26	6	5	14.1	23.72 S	179.67 W	4.9	507
291	ISC	1984	12	28	15	59	48.8	23.50 S	179.14 E	5.2	554
292	ISC	1985	2	21	6	56	3.2	23.91 S	179.78 W	5.1	531
293	ISC	1985	3	14	6	26	58.9	23.70 S	179.92 W	5.0	522
294	ISC	1985	6	7	16	12	35.9	23.81 S	179.81 W	5.1	501
295	ISC	1985	7	10	16	33	28.3	23.64 S	178.85 E	5.0	551
296	ISC	1985	8	2	3	5	48.2	24.38 S	179.81 E	5.1	515
297	ISC	1985	10	13	14	13	36.0	25.17 S	179.90 E	5.1	494
298	NEIS	1986	2	20	5	37	59.1	24.97 S	179.72 E	4.7	505
299	ISC	1986	2	20	16	6	36.2	23.55 S	179.84 W	5.2	552
300	ISC	1986	6	12	10	34	52.0	25.15 S	179.73 E	5.0	510
301	NEIS	1986	7	17	2	47	5.1	23.57 S	179.96 E	4.7	550
302	NEIS	1986	7	24	11	11	41.6	23.41 S	179.83 E	4.9	548
303	NEIS	1984	5	18	11	55	29.2	24.95 S	179.62 E	4.7	516
304	NEIS	1984	5	20	7	22	45.1	24.26 S	179.76 W	4.9	527
305	NEIS	1980	7	15	17	4	21.6	23.48 S	177.30 W	4.8	201

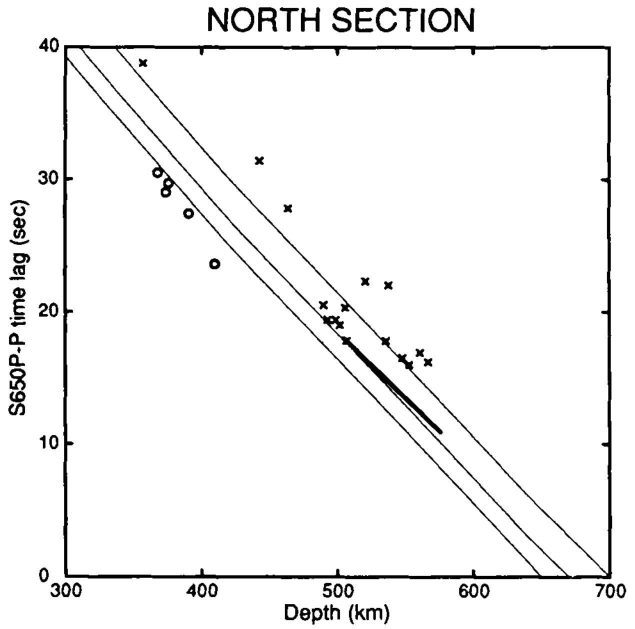

Figure 6. Plot of $S_{670}P$–P delay as a function of focal depth. The thin lines are theoretical curves calculated from PEMC for S–P conversion at 650, 670, and 700 km depth. Open symbols are from Barley *et al.* (1982), and × are from Bock & Ha (1984). The heavy line represents our best results from the North section of Tonga.

P-wave amplitude. The normalization prevents a bias toward the largest events. We have discarded a few events with extremely noisy codas—these are generally the smaller earthquakes ($m_b \leq 4.9$) that are just above the detection threshold.

There are three coda phases after the initial P-wave. The phases at about 90 and 120 s after P, are, respectively, PcP and PP as indicated in Fig. 9(a). The other phase shows the appropriate arrival-time dependence on hypocentral depth for $S_{670}P$. In these linear stack sections the three coda phases are all quite subtle, especially $S_{670}P$.

A hypocentral depth section of nonlinear single-event stacks is shown in Fig. 11(a). Here we have used 4th root stacks, and we have used the 'time average product' method to further discriminate against spurious signals. We form the nonlinear stack for each arm of the array, then we take the square root of the product of the two stacks at each time point, again preserving the sign. This allows signals that arrive simultaneously on the N–S ('blue') arm to remain prominent only if they arrive with the correct slowness across the E–W ('red') arm—only the E–W arm can discriminate effectively according to slowness, because it is pointed toward the earthquake sources in Tonga. Also, we reject any negative products as noise, since both arms of the array should have the same polarity for coherent arrivals. All of these procedures are designed to emphasize coda phases of the desired slowness and azimuth. Finally, the

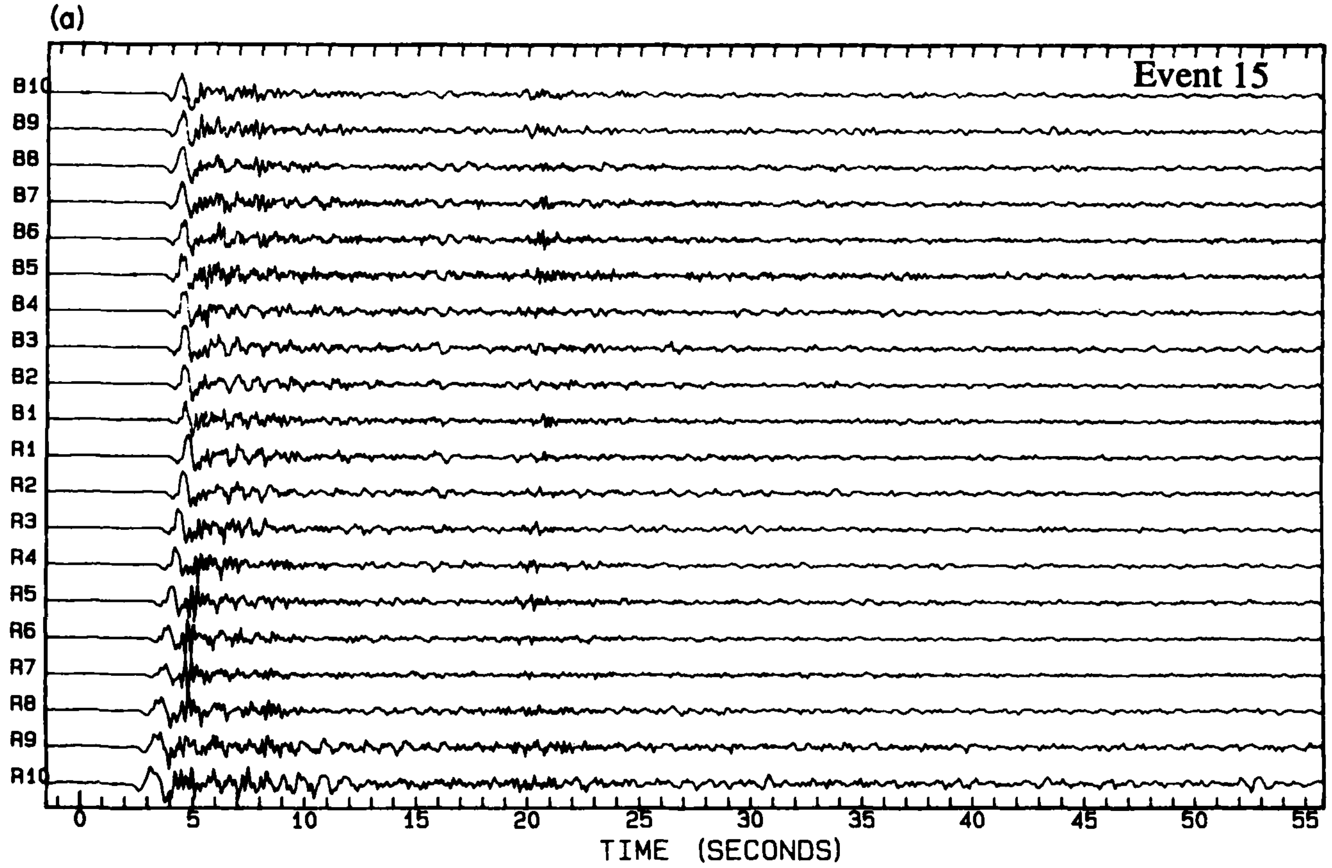

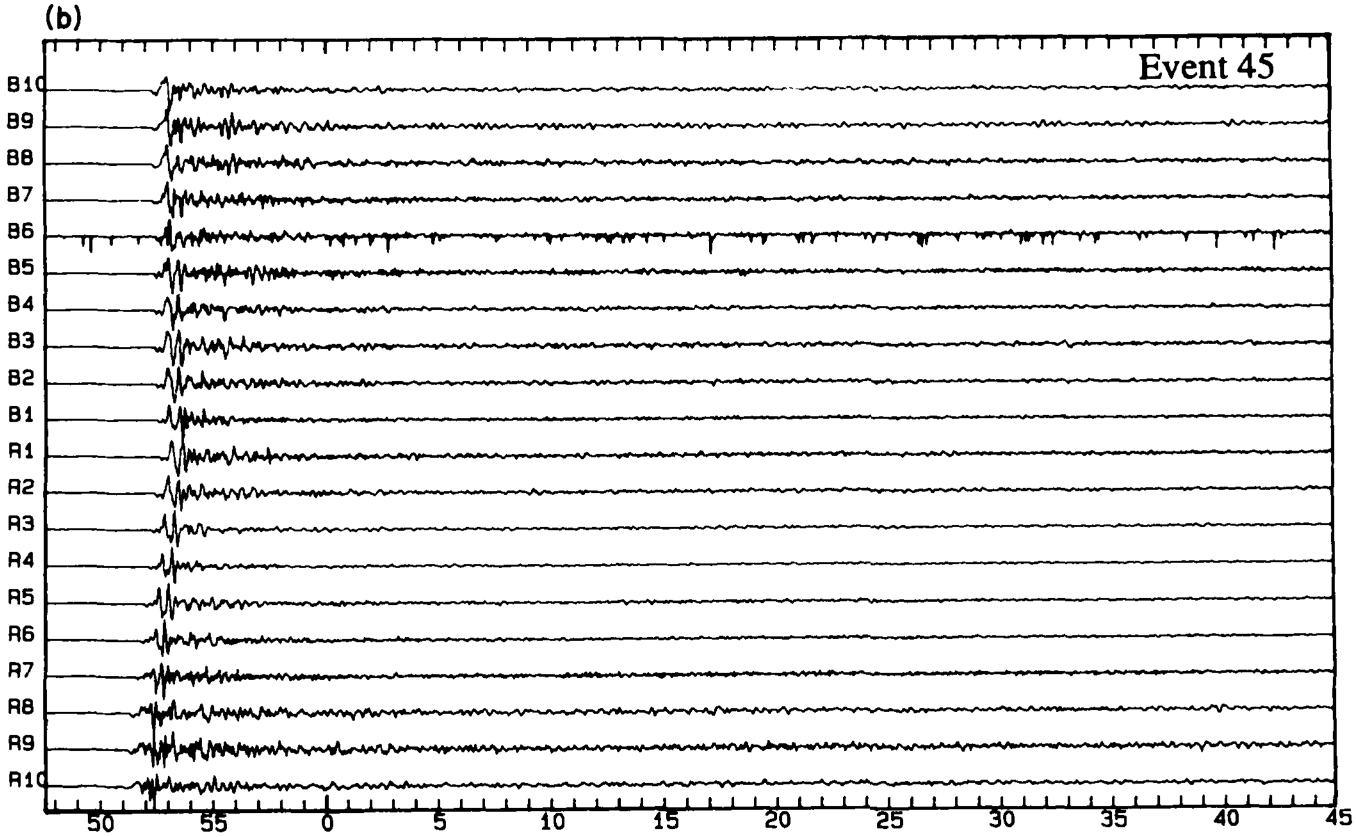

Figure 7. (a) Vertical component seismograms from WRA for event no. 15. See Fig. 2 for station locations. (b) Vertical component seismograms from WRA for event no. 45. Channel B6 is malfunctioning and is excluded during the stacking phase (Figs 8 and 9).

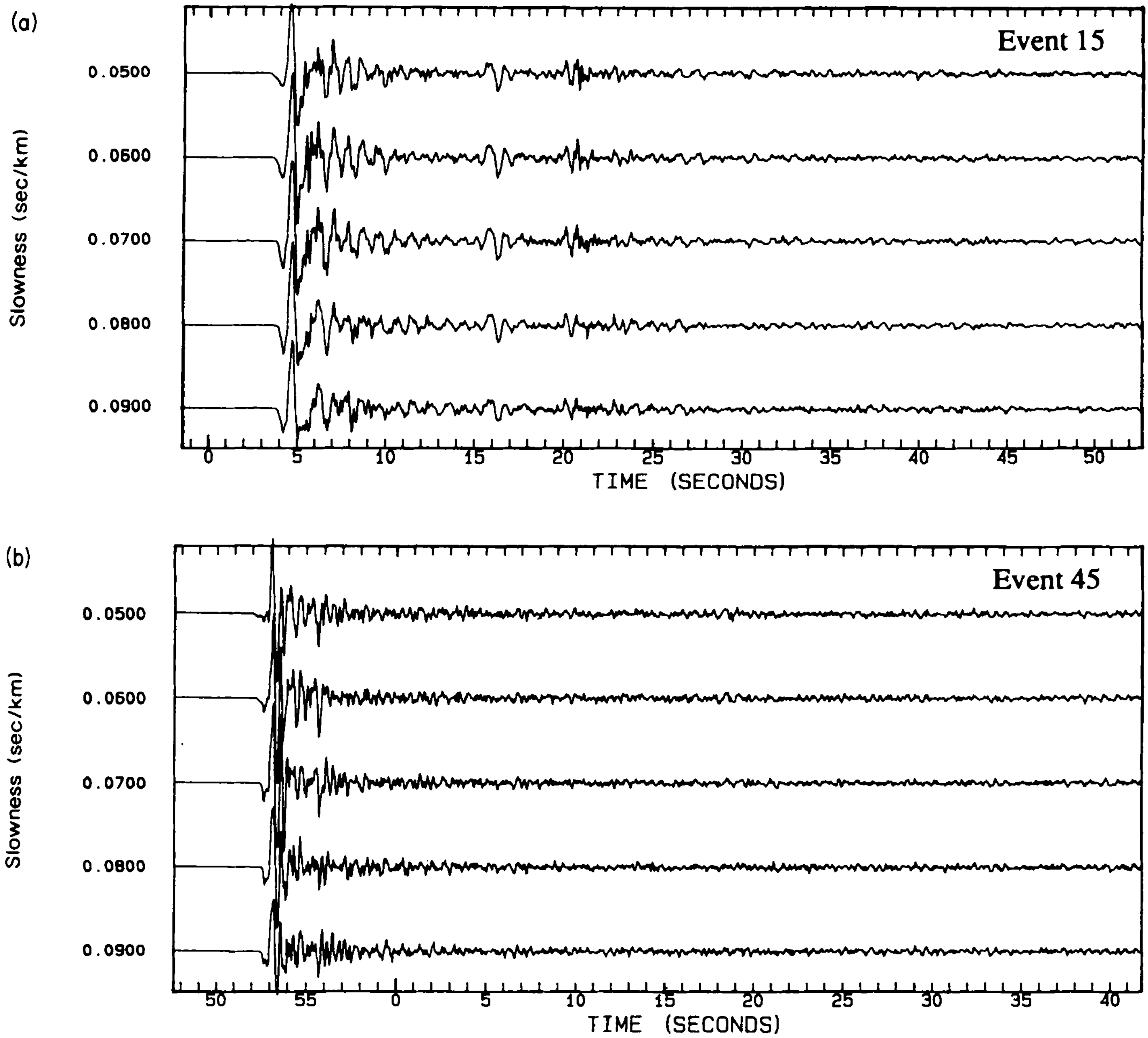

Figure 8. (a) Linear stacks for event no. 15 for slownesses from 0.05 to 0.09 s km^{-1} across WRA. The correct source–receiver azimuth (274°) is used to phase the array. (b) Same as in Fig. 8(a), but for event no. 45.

resultant stacked traces are smoothed by a half-second moving average window.

The $S_{670}P$-phase is much more prominent in the nonlinear section of Fig. 11(a) than in the linear section of Fig. 10(a). By contrast, the *PcP*-phase is more subdued because its slowness (~0.03 s km^{-1}) is quite different from the stacking slowness (~0.07 s km^{-1}) used to enhance $S_{670}P$. This dramatically illustrates the effectiveness of the nonlinear stacking method compared to the linear method. From the nonlinear section, we note several interesting observations: (1) The amplitude of $S_{670}P$ is comparable to that of the phase *PP*—since the slowness of *PP* (~0.089 s km^{-1}) is similar to *P*, it is nearly optimized by the stacking procedure. (2) $S_{670}P$ is much stronger for some events (seven in particular) than others, and it is more intermittent in occurrence than *PcP* and *PP*. (3) $S_{670}P$ appears most clearly for hypocentral depths between about 500 and 600 km, although observation is hindered by the small number of shallower events and by interference with the *P*-wave itself for deeper events.

4.3 Hypocentral depth sections: Central and South Tonga

Sections of nonlinear stacks from Central and South Tonga are shown in Figs 11(b) and (c). Each section consists of about 100 events which are processed in the same way described above for the North section. The Central section does not show a distinct $S_{670}P$ phase, although there are various signals within 20–40 s of *P*. There are relatively few

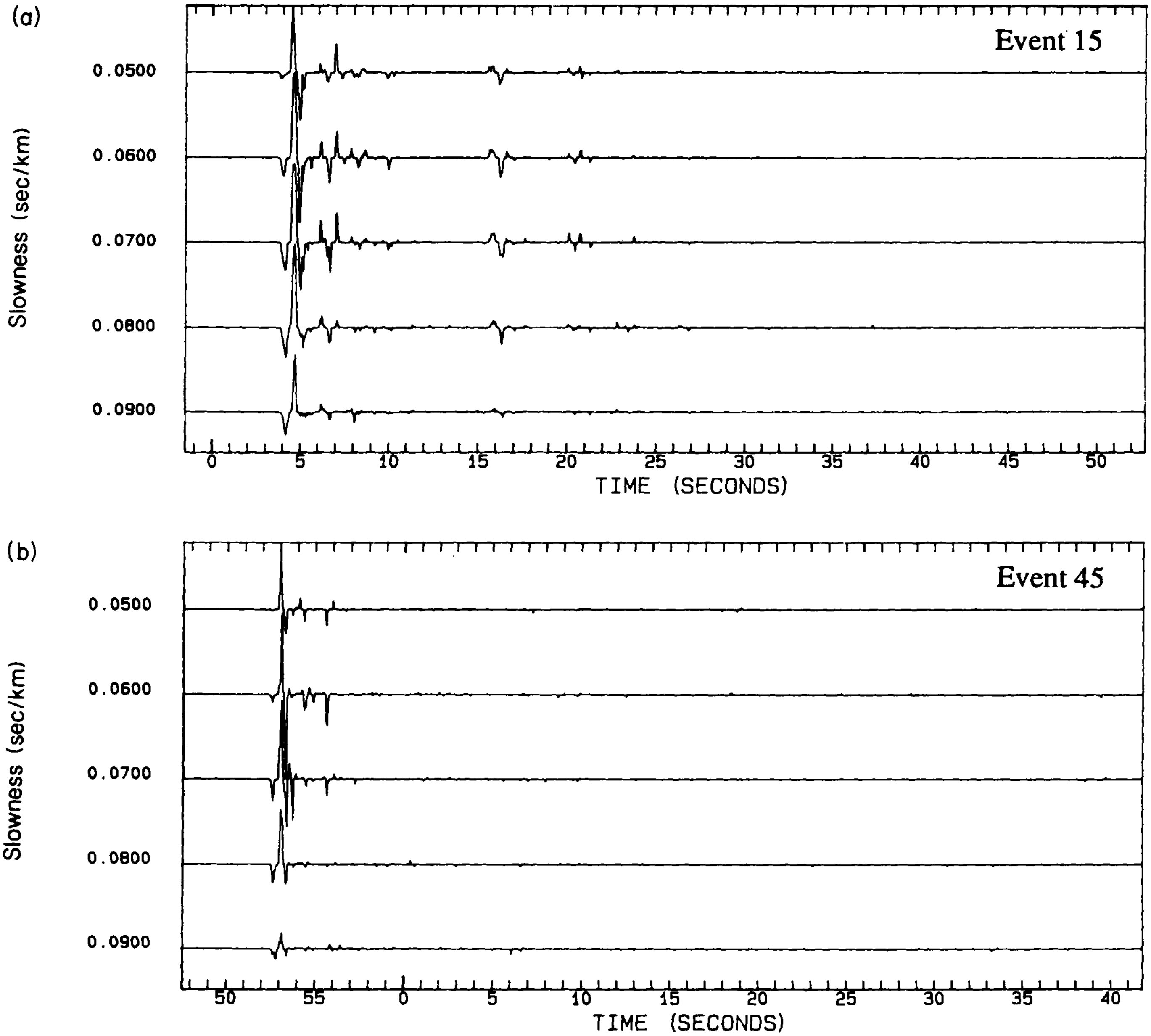

Figure 9. (a) Nonlinear stacks for event no. 15 using the *n*th root method of Muirhead & Datt (1976). Otherwise, same as Fig. 8(a). (b) Same as Fig. 9(a), but for event no. 45.

events in the depth range 525 km to 575 km in which most of the $S_{670}P$ arrivals occur for the North section, so we cannot firmly conclude that the converted phase is absent beneath the Central section.

In the South section (Fig. 11c), there is an $S_{670}P$ phase similar to that found in the North. However, only five or six events show the phase clearly, and there are slightly later arrivals which complicate the picture. In fact, there is a hint of a second arrival following $S_{670}P$ by about 5 s. Except for a rather noisy event at about 460 km depth, this second arrival does not consistently occur along with $S_{670}P$ on single events. The $S_{670}P$ phase indicated by the arrow in Fig. 11(c) has the appropriate hypocentral depth dependence of arrival time delay relative to *P*. Note also that for both the Central and South sections, the *PP* phase is much less distinct than for the North section.

4.4 Slant-stacks

The most important characteristic of $S_{670}P$ is its delay relative to *P* as a function of hypocentral depth. Theoretically this relationship is almost linear for laterally homogeneous earth models (Fig. 6), with a slope of about $-0.11\,\mathrm{s\,km^{-1}}$ (of focal depth). The easiest way to 'see' $S_{670}P$ in Fig. 11 is to place one's eye close to the page and site along the slope of the phase in section. This tool can be formalized by slant-stacking through the focal depth sections. The focal depth dependence and arrival times of various phases can be measured by slant-stacking over a range of slope and determining which slope maximizes a given phase.

Slant-stacks for North Tonga are shown in Fig. 12(a). Time, relative to *P* for a reference event depth of 550 km, is

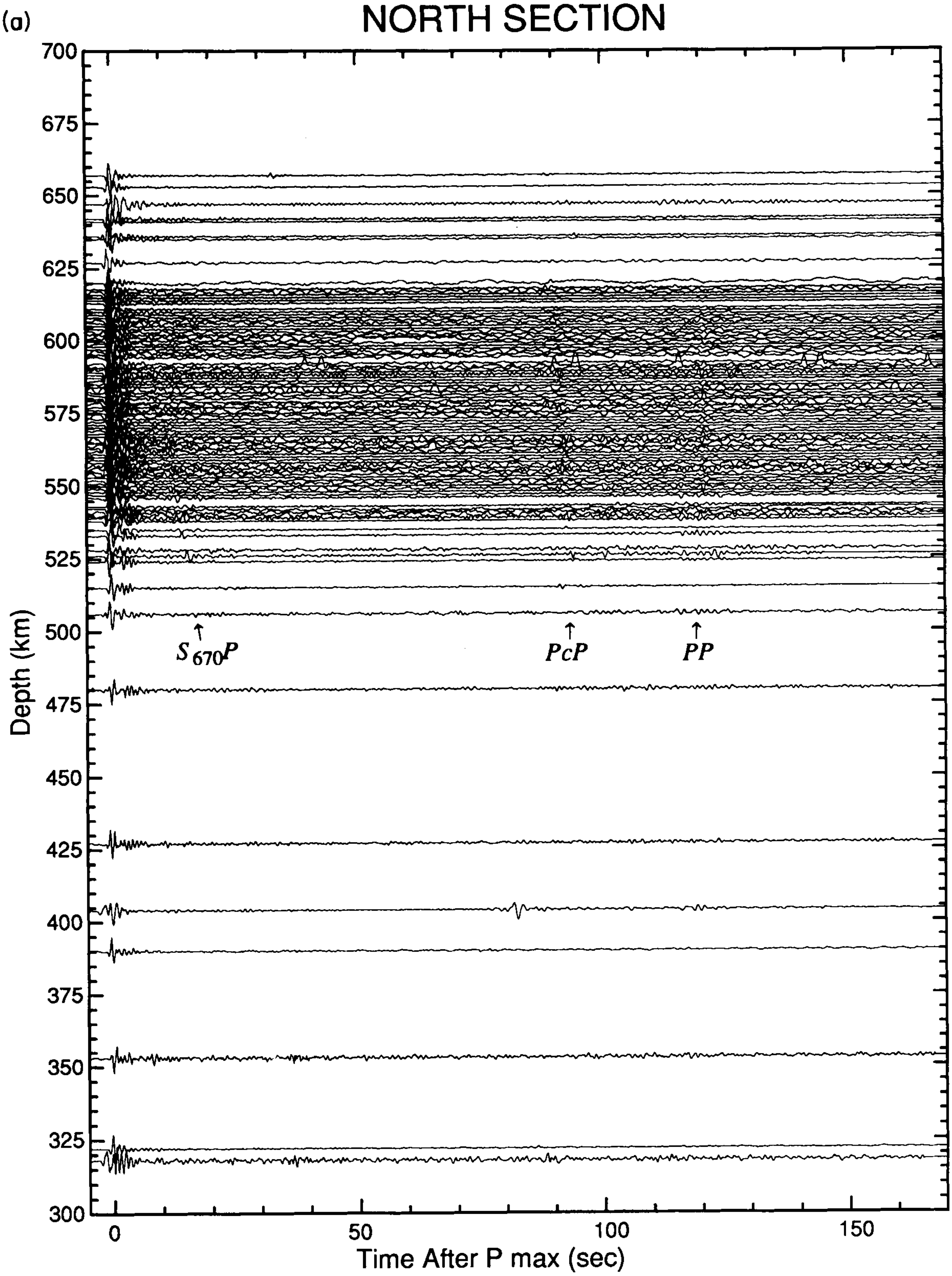

Figure 10. (a) Linear stack section for North Tonga. Traces are aligned so that maximum P amplitude falls at $t = 0$ on the time axis. Focal depth is plotted on the vertical axis (see Table 1). PP, PcP, and $S_{670}P$ phases fall along directions of arrows. (b) Linear slant-stacks for North Tonga. Slope corresponds to lines through the focal depth section of Fig. 10(a) for slant-stacking. Time is relative to the P arrival for a reference focal depth of 550 km. The amplitude has been magnified by a factor of 10 following the P arrival by 10 s to emphasize coda phases.

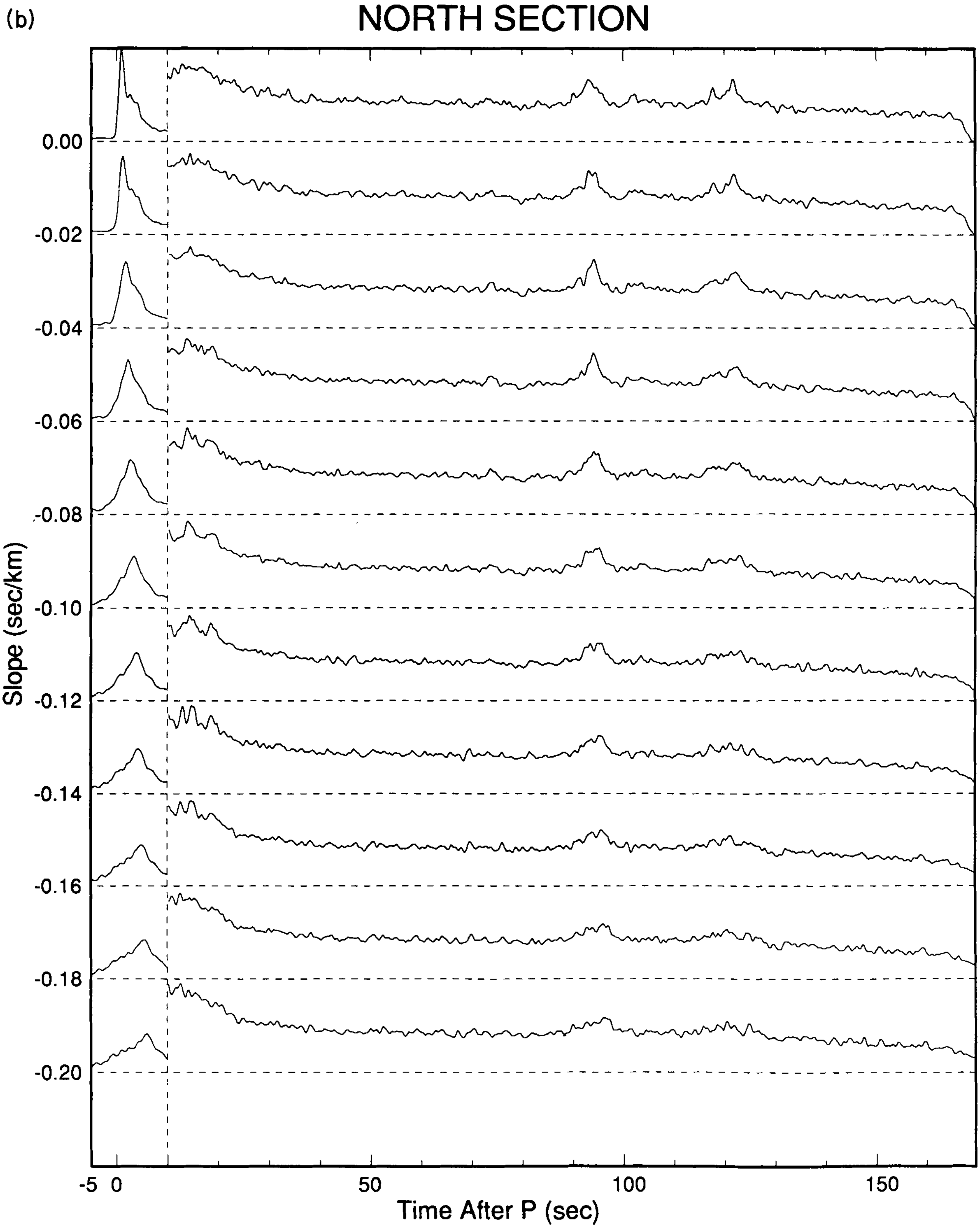

Figure 10. (*continued*)

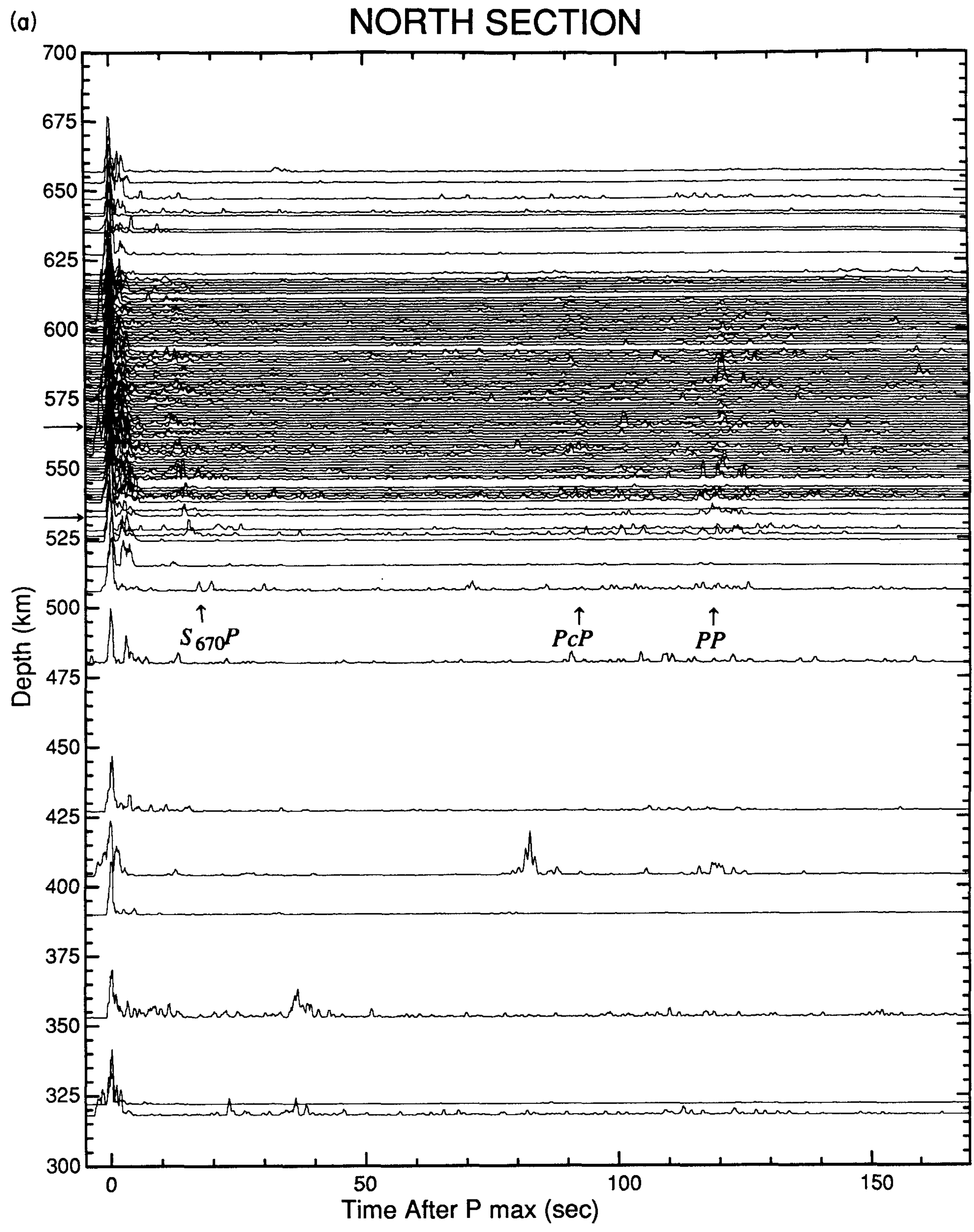

Figure 11. Nonlinear stack sections for (a) North Tonga, (b) Central Tonga, and (c) South Tonga. In (a) the arrows on the depth axis indicate the events shown in the TCT array recordings of Fig. 15.

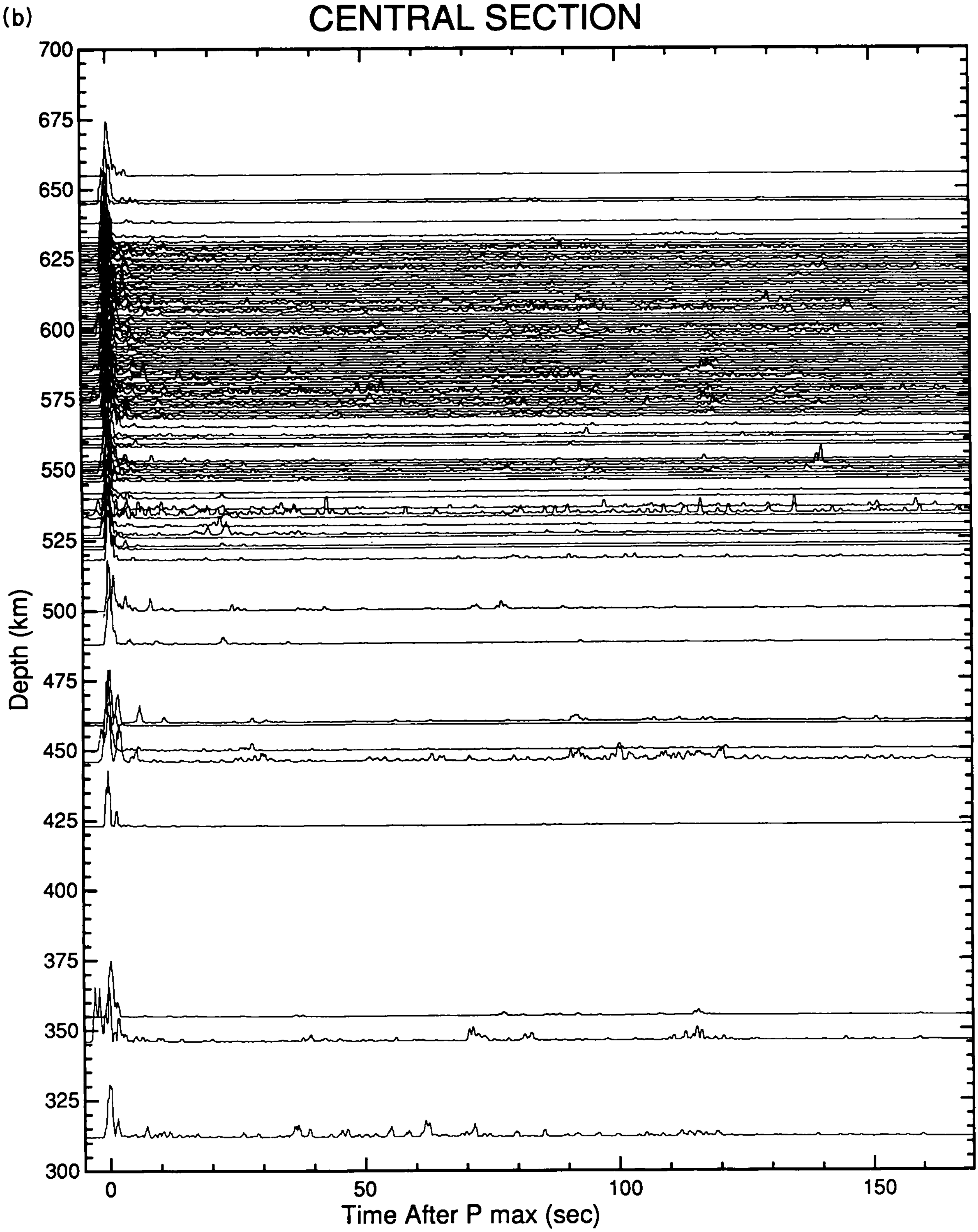

Figure 11. (*continued*)

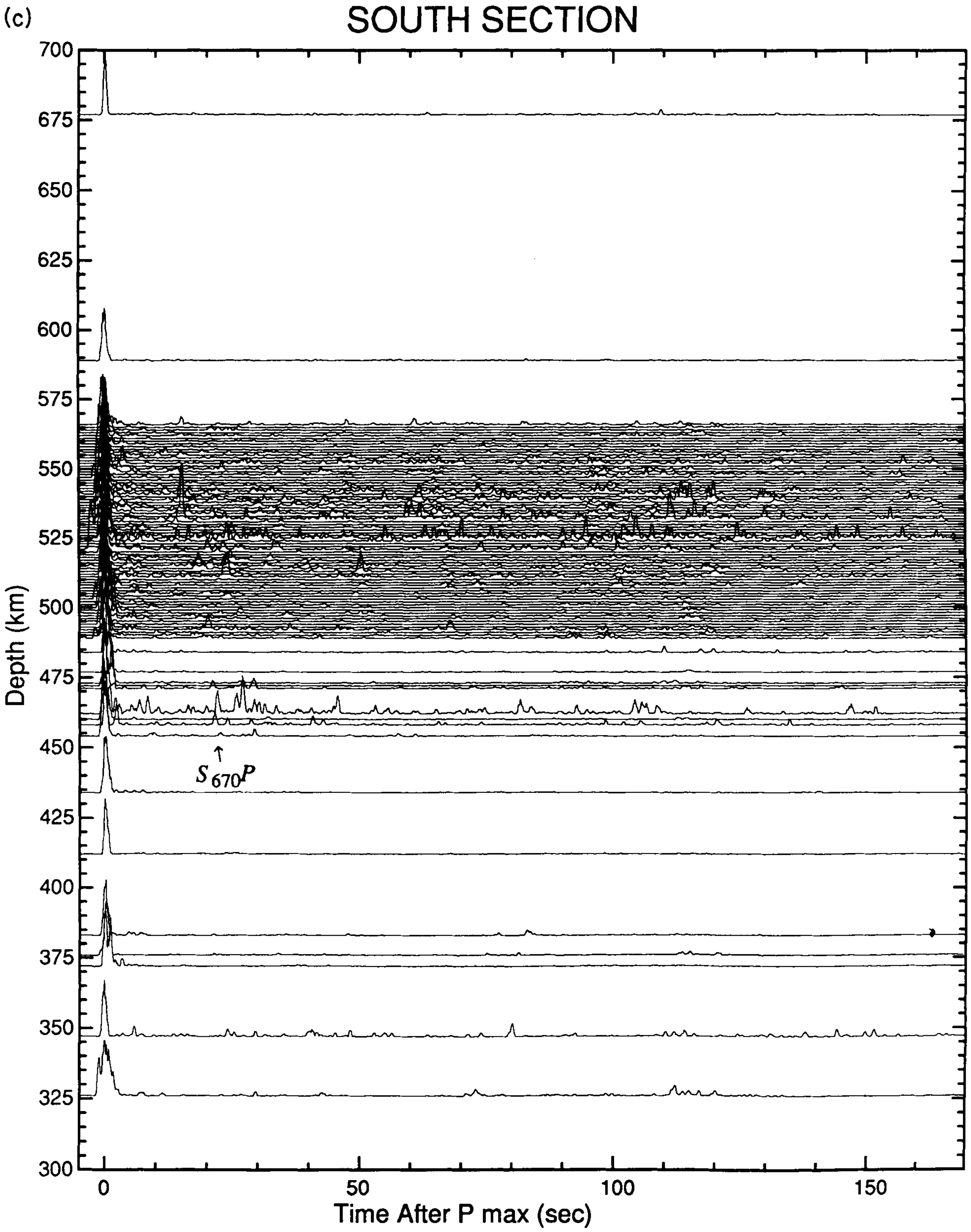

Figure 11. (*continued*)

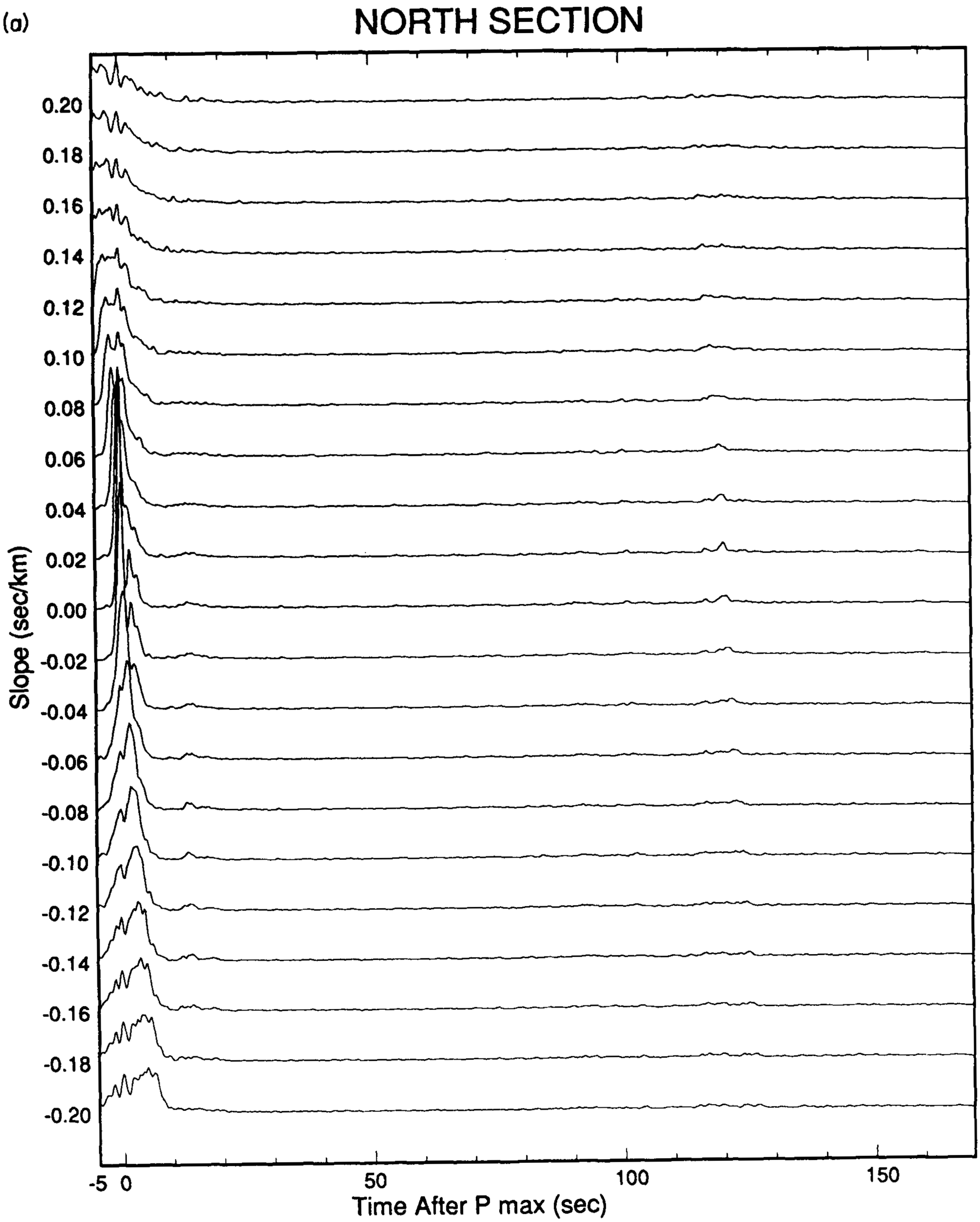

Figure 12. Nonlinear slant-stacks for (a) North Tonga, (b) Central Tonga, and (c) South Tonga.

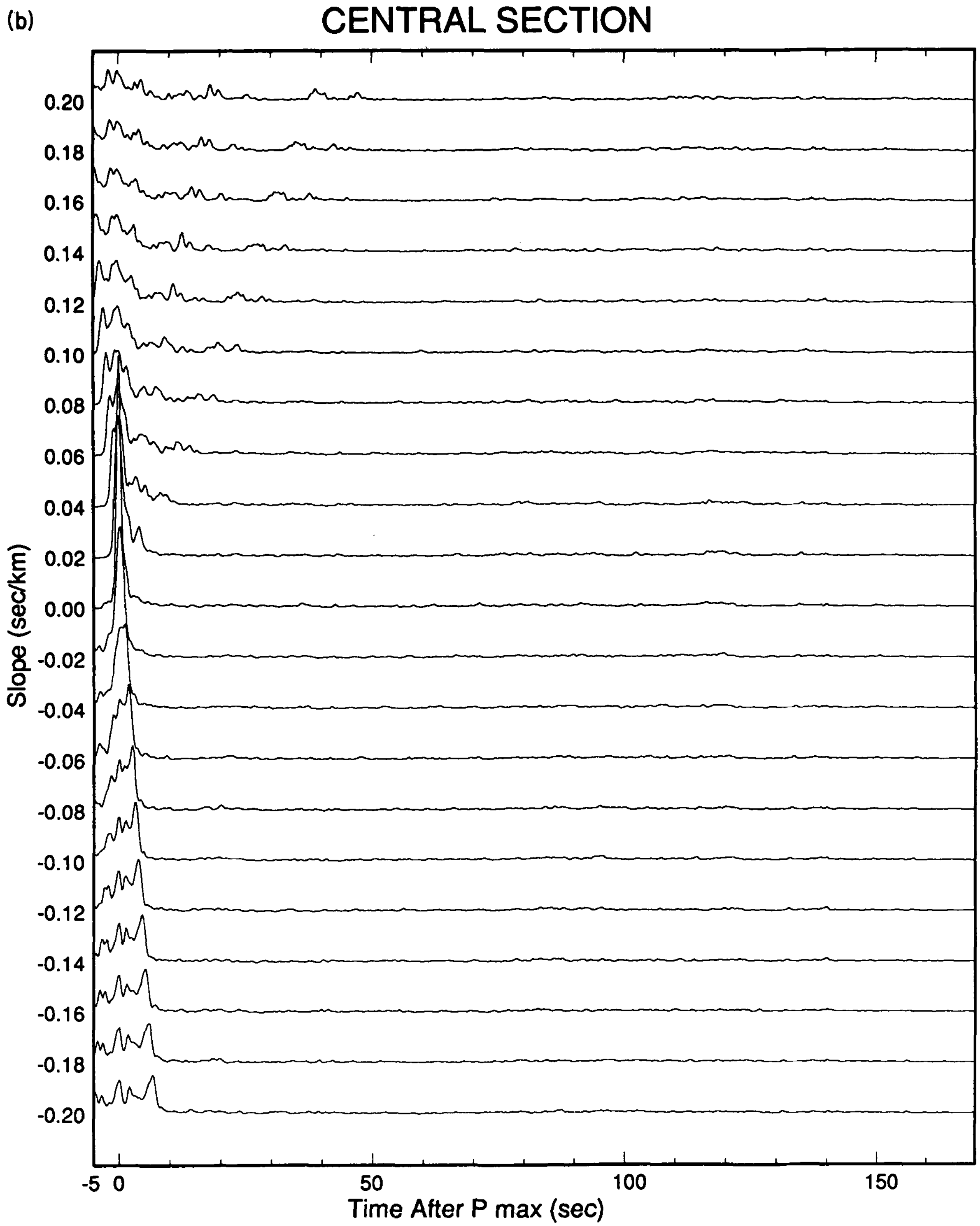

Figure 12. (*continued*)

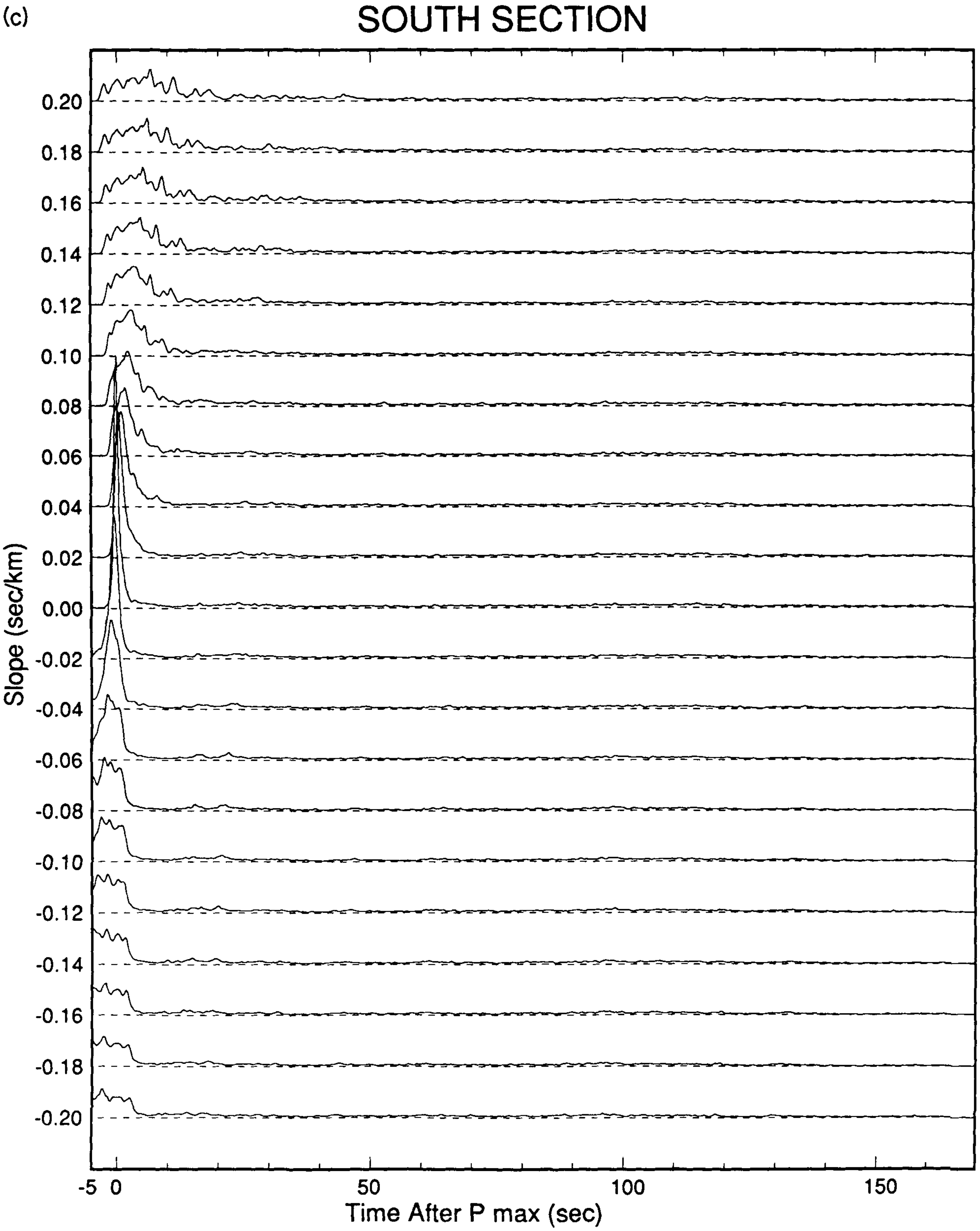

Figure 12. (*continued*)

plotted on the horizontal axis. The slant-stacking slope is swept over values from +0.20 to $-0.20\,\mathrm{s\,km^{-1}}$ (of focal depth), and plotted on the vertical axis. Only events between 450 km and 585 km depth are included in the slant-stacks in order to focus on the depth interval of interest in Fig. 11(a). The large arrival at about 120 s is *PP*. The 'bump' just after *P* is $S_{670}P$. The amplitude of $S_{670}P$ is maximized for a slope of about $-0.10\,\mathrm{s\,km^{-1}}$. Theoretically the slope should be about $-0.11\,\mathrm{s\,km^{-1}}$ for a flat discontinuity. The travel time delay for $S_{670}P$ relative to *P* is about 13.5 s at the reference focal depth of 550 km, so this phase would plot along the 6 km line Fig. 6.

A more detailed look at the $S_{670}P$ peak is given in Fig. 13(a), where the slant-stack amplitudes are magnified by a factor of 30 just after the large amplitude *P*-wave arrival. The sharp peak at $-0.10\,\mathrm{s\,km^{-1}}$ is remarkably well-defined, as are the peaks corresponding to *PP* (~120 s after *P*, $0.0\,\mathrm{s\,km^{-1}}$) and, to a lesser extent, *PcP* (~90 s after *P*). Other small bumps in the slant-stacks from the North section are mainly from single event signals, as can be seen by detailed inspection of Fig. 11(a).

Slant-stacks for the Central and South sections are shown in Figs 12(b) and (c), and magnified versions are shown in Figs 13(b) and (c). The depth interval for slant-stacking both of these sections is 300 to 585 km. The spurious signals in the upper lefthand corners of Figs 12(b) and (c) are caused by spillover of *P*-waves from shallower events, hence their strong moveout in the slant-stack sections.

For the Central section (Figs 12b and 13b) there is almost no indication of coherent arrivals in the slant-stacks. There is a small peak following *P* by about 12 s for a slope of $-0.08\,\mathrm{s\,km^{-1}}$, but it is no more convincing than the event section of Fig. 11(b). For the South section (Figs 12c and 13c) there are two peaks in the slant-stacks following *P* by about 16 and 21 s. The slope maximizing these two peaks lies between −0.06 and $-0.12\,\mathrm{s\,km^{-1}}$. This is the double arrival referred to in the previous discussion of Fig. 11(c). If these peaks are *S–P* conversions, they correspond to conversion depths of about 680 and 720 km—somewhat deeper than for the North section.

The phases which are obvious in Figs 12 and 13 are just as obvious in the event sections of Fig. 11, and the slant-stacks serve mainly to measure the focal depth dependence of various coda phases. The results of this section can be summarized quite concisely by returning to the type of delay *vs.* focal depth plot we used in Fig. 6. In Figs 14(a) and (b) the theoretical curves for *S–P* conversions from 650, 670, and 700 km depth are shown by dots which correspond to actual events from the North and South sections, respectively. This emphasizes how the data density varies with focal depth. The heavy dashed lines show our best estimates for $S_{670}P$ phases from the slant-stacks. These lines span only the depth ranges over which the phases can be clearly seen in the event sections. (Note that we have used straight lines for slant-stacking, while the lines in Fig. 6 are slightly curved. Since the observed $S_{670}P$ phases only occur mostly in the small depth interval of 450–575 km, this is a satisfactory approximation.)

For the North section (Fig. 14a), the apparent conversion depth is between 650 and 680 km for event foci between 500 and 575 km depth. For the South section (Fig. 14b), the apparent conversion depth of the first arrival phase is between 650 and 690 km for event foci between 450 and 550 km depth. The second arrival, which we regard as much more tenuous, corresponds to a depth range about 40 km deeper. No clear $S_{670}P$ phase is observed in the Central section.

4.5 Comparison with a large aperture array

We have concentrated on a very dense data set from a single, medium aperture array (WRA). There is, of course, an enormous amount of data available from other seismographic stations for the more than 300 earthquakes we have used. Although we are now using WWSSN recordings from the Southwest Pacific area to study radiation pattern effects (see discussion below), it is impractical to exploit all the available data at this time. However, a unique seismic array experiment conducted in northern Australia during the time period covered by our study yields an interesting comparison and is a potential guide to future studies,

From June 1979 to November 1979, the Australian National University deployed a temporary array of short-period vertical seismometers (the 'TCT' array) across northern Australia from Tennent Creek, Northern Territory (the location of WRA) to Townsville near the coast of Queensland. The stations are shown by triangles in Fig. 1. This array covered an east–west distance of 1000 km, and is ideally located to detect $S_{670}P$ from Tonga (although it was not designed specifically for that purpose).

The TCT array experiment recorded some of the same deep Tonga events used in our study. Two of these events in particular (from the North Tonga section) show very prominent $S_{670}P$-phases on the WRA recordings. Nonlinear stack traces from WRA for these two events (numbers 15 and 16, Table 1) are indicated by arrows on the depth axis in Fig. 11(a). The TCT recordings are shown in Fig. 15, with epicentral distance on the vertical axis. The traces have been time shifted according to the expected arrival time at each station.

The arrival times of the strongest coda phases from nonlinear stacks of the WRA recordings are given by arrowheads on the time axes in Fig. 15. In Fig. 15(a) at least a few of the seismograms show a clear phase at the predicted time, about 17 s after *P*. In Fig. 15(b) the phase is present on at least eight of the 12 traces, particularly TCT02 through TCT12. Both of these sets of recordings show that the $S_{670}P$-phase is present over a large epicentral distance range. Also note that $S_{670}P$ shows almost constant delay with respect to *P*, which is expected since the two phases have almost identical slowness.

These results are not surprising, but serve to reinforce our interpretation of the *X*-phase as $S_{670}P$. Since $S_{670}P$ from deep earthquakes has been previously reported only for WRA recordings (i.e., Barley *et al.* 1982; Bock & Ha 1984), it is good to note that there is nothing peculiar about the ability of WRA to detect these phases. Also, with the recent initiatives in the seismological community for large temporary array experiments (e.g. PASSCAL), these examples from the TCT experiment may provide inspiration for future large aperture teleseismic array studies.

5 DISCUSSION

This study demonstrates the observability of $S_{670}P$ for events beneath Tonga, and our results can be summarized as

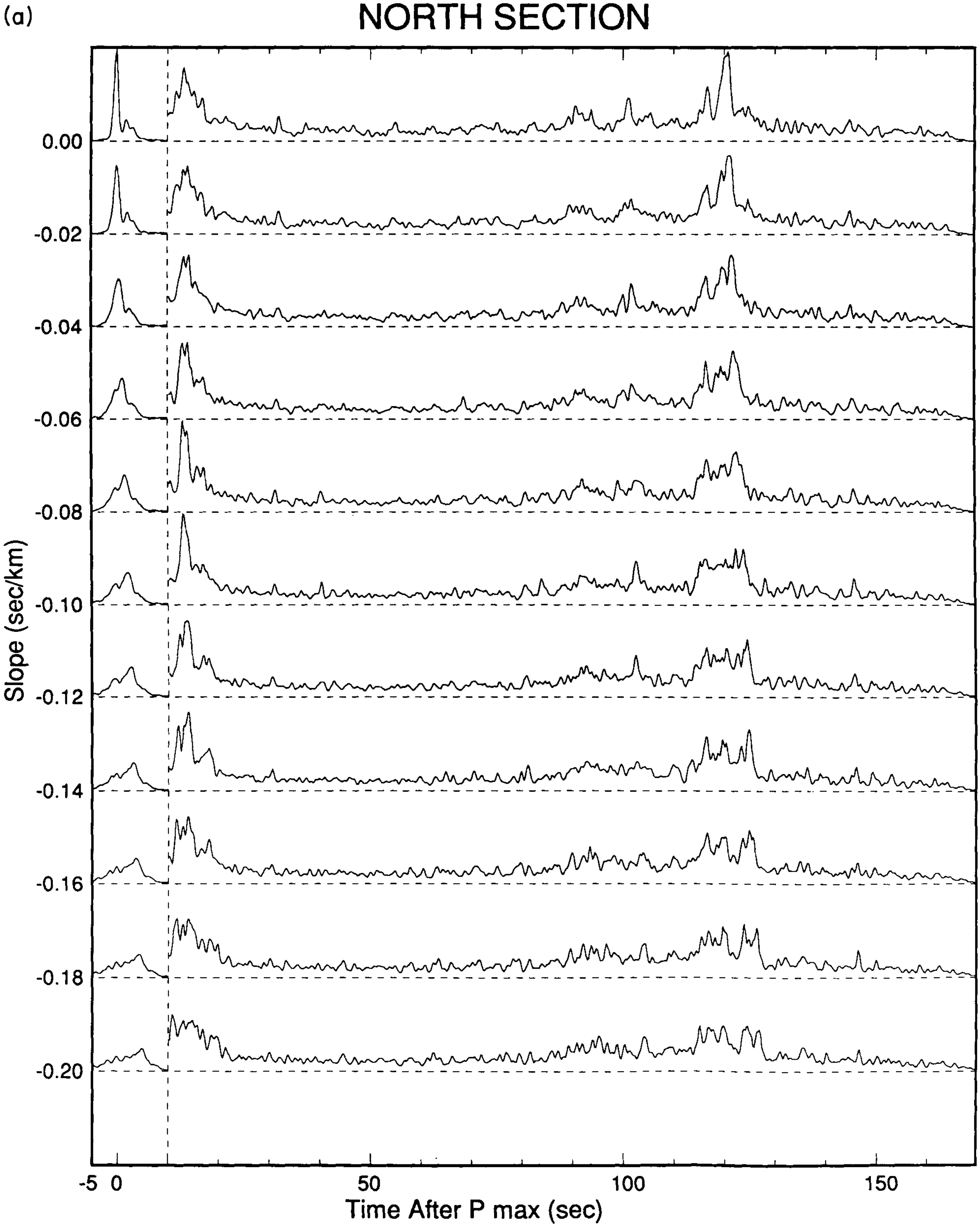

Figure 13. (a), (b), and (c) Same as Fig. 12 except that the amplitude has been magnified by a factor of 30 following the *P* arrival by 10 s to emphasize the coda phases.

(b)

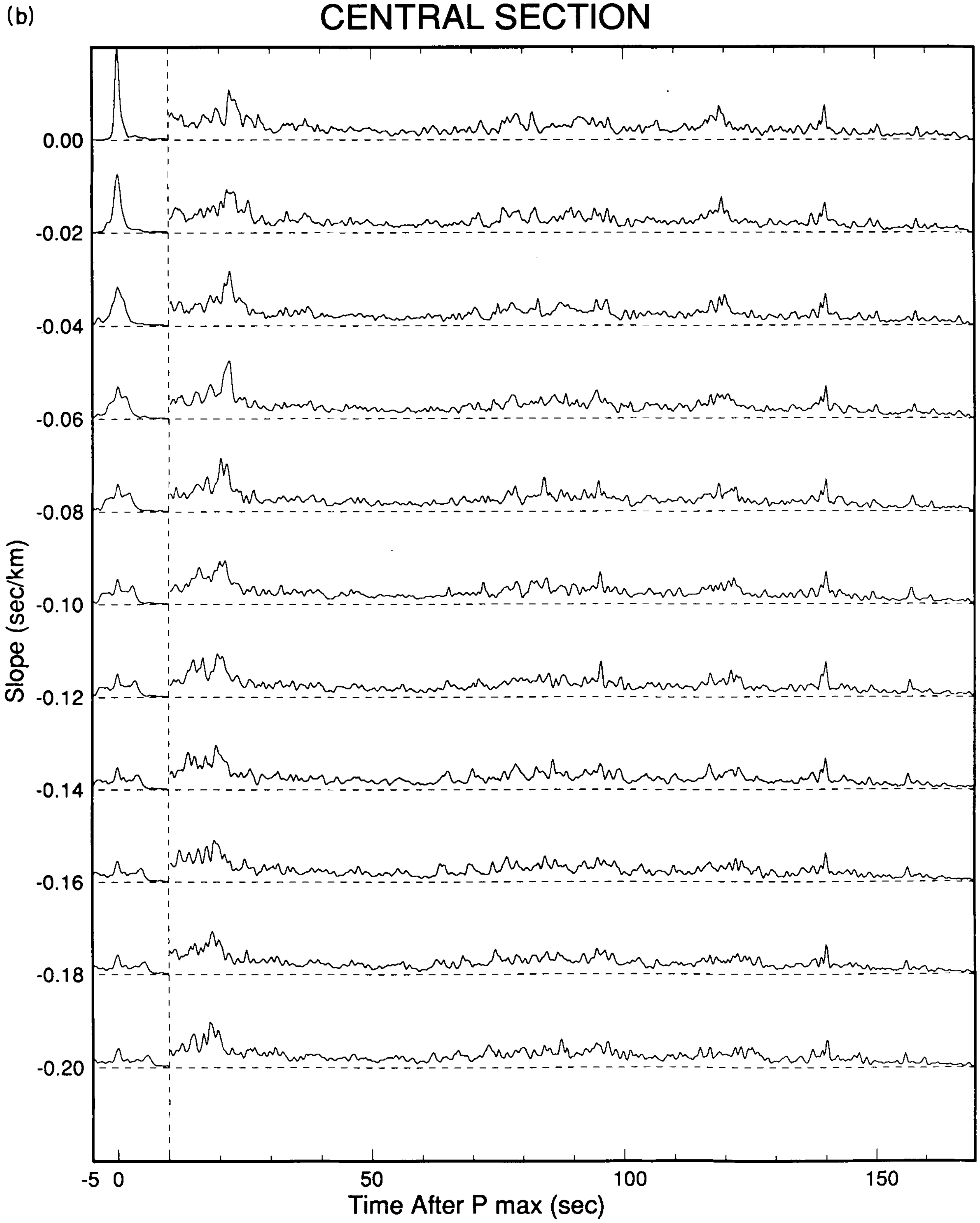

Figure 13. (*continued*)

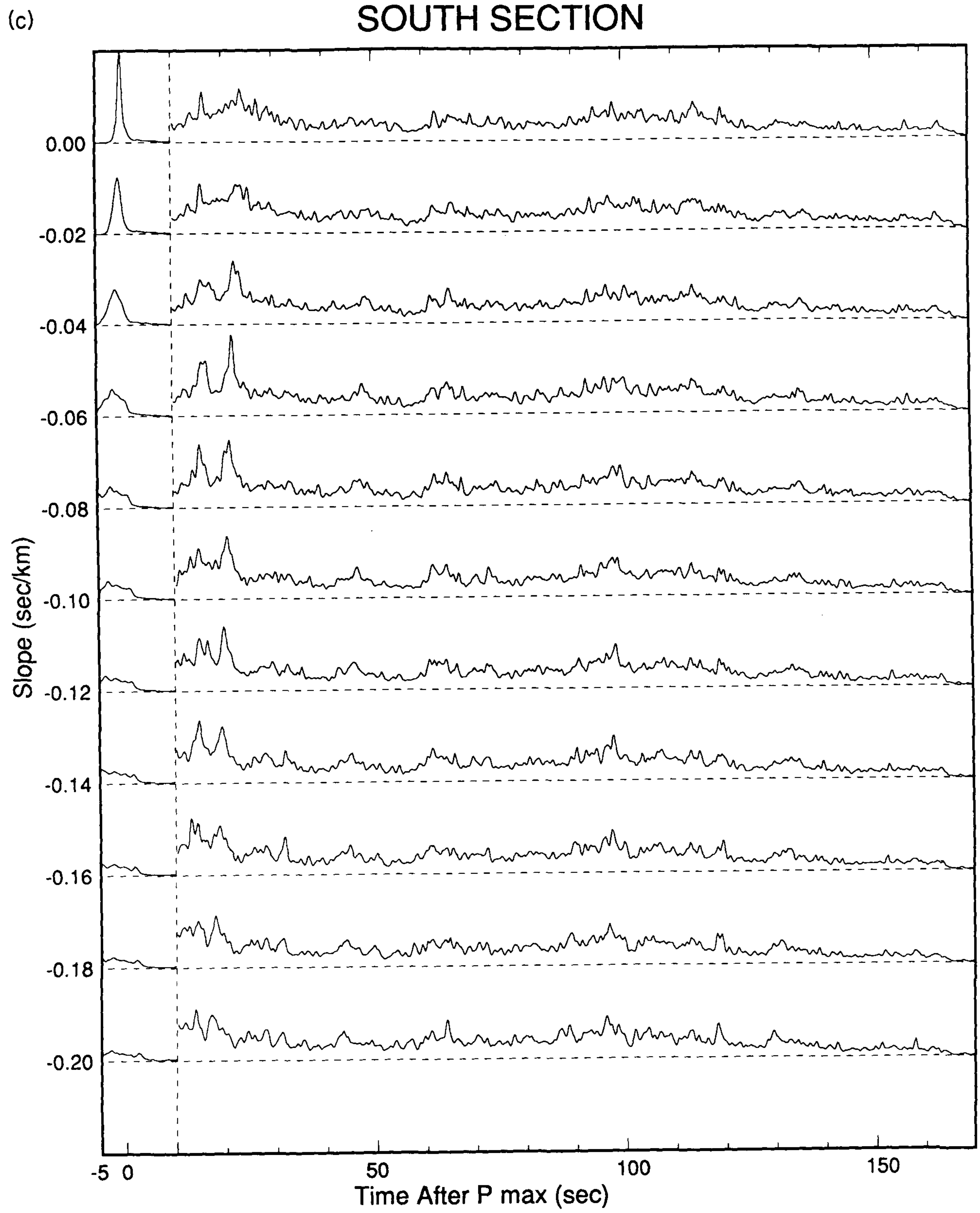

Figure 13. (*continued*)

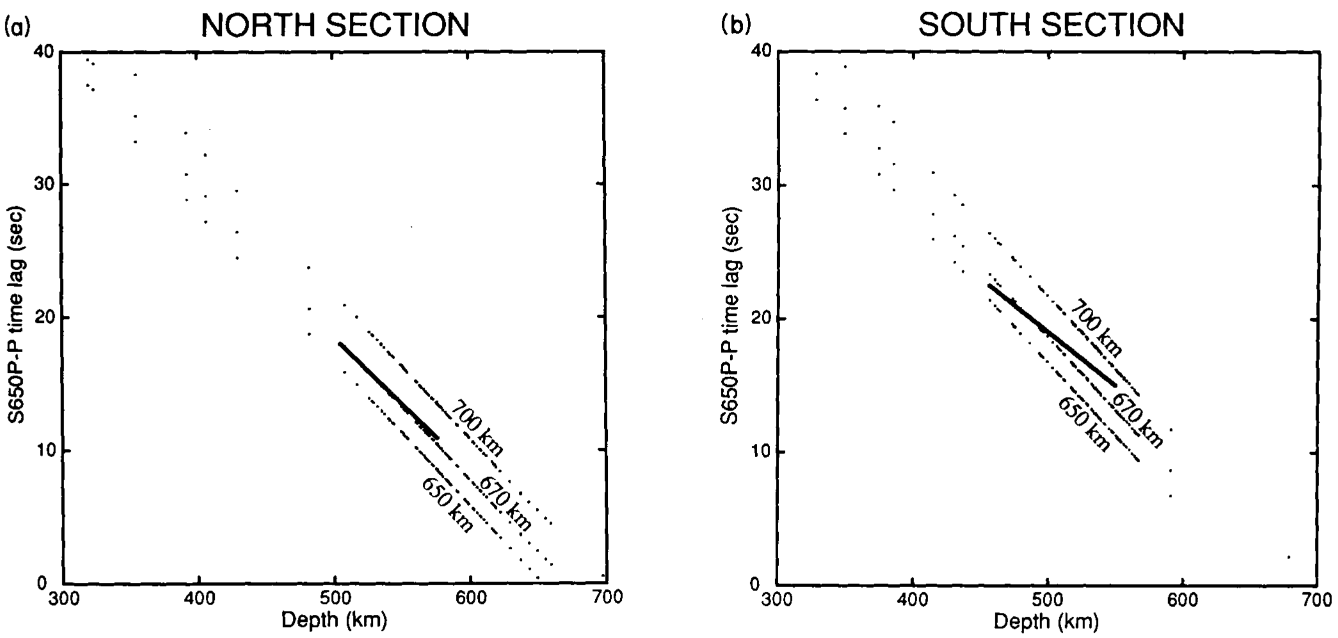

Figure 14. (a) Delay *vs.* focal depth plot for North Tonga. Dots correspond to the theoretical $S_{670}P-P$ delays (calculated from PEMC) for individual events from the North section. The resulting three dotted lines are for $S-P$ conversion depths of 650, 670, and 700 km. The solid line is our best estimate of delay *vs.* depth from the North section slant-stacks for the events clearly showing $S_{670}P$ between 500 and 575 km focal depth. (b) Same as Fig. 14(a), except for South Tonga. The solid line is our best estimate for delay *vs.* depth for events between 450 and 550 km focal depth.

follows: (1) For North Tonga the $S_{670}P$-phase is clear for events between 500 and 575 km focal depth, with apparent conversion depths between 650 and 680 km. (2) For Central Tonga the phase is largely absent. (3) For South Tonga there are, perhaps, two $S-P$ coda phases. The first is probably $S_{670}P$ occurring for events between 450 and 550 km focal depth, with apparent conversion depths between 650 and 690 km. The second phase may be an $S-P$ conversion from about 690 to 730 km but is much less distinct. (4) Because the conversions occur at short period, the 670 km discontinuity must be sharp (less than ~5 km transition interval). (5) The $S-P$ conversions occur either within or adjacent to the subducted Tonga slab, implying little deformation or warping of the discontinuity in that zone.

One possible further interpretation deserves mention. We note from Fig. 14 that the slopes for delay *vs.* focal depth we have measured are less negative than predicted by simple seismic velocity models (especially for the South section). This could result from a 20–40 km depression in the 670 km discontinuity within the slab, since this would explain why deeper earthquakes show somewhat larger delays than expected—$S-P$ rays from deeper earthquakes have less chance of escaping the slab before mode conversion takes place. If we further assume that this depression of the 670 km discontinuity results from the relatively cold slab temperature, then a phase transition with a small, negative Clapeyron slope is implied.

Not surprisingly, our study raises more questions than it answers, and our interpretations are subject to qualification. We still need to address the following problems: (1) We have obtained somewhat different results than Bock & Ha (1984) for South Tonga. (2) Uncertainties in focal depth determinations by the ISC and NEIS may affect the apparent $S-P$ conversion depths. (3) Although the intermittent occurrence of $S_{670}P$ can be explained in terms of variations in source radiation patterns, we eventually need to verify independently that this is indeed the case. Reliable estimates for $S-P$ transmission coefficients cannot be made unless the radiation pattern problem is solved. (4) Lateral heterogeneity near and within the subducted slab will affect the raypaths and travel time delays in ways that are difficult to model without better knowledge of the seismic structure beneath Tonga.

Most of these issues were touched upon by Bock & Ha (1984), including a detailed treatment of transmission coefficients. Here we address these problems briefly in order to show that only minor modifications of our conclusions are likely to result from more thorough studies.

5.1 Comparison with previous results

Our results, at least for the North section, are compatible with those of Barley *et al.* (1982) from the Izu-Bonin arc. They found apparent conversion depths of about 650 km for events between 350 and 450 km focal depth (Fig. 6). The $S_{670}P$ raypaths from the Izu-Bonin arc travel more or less along the strike of the subducting slab, which dips toward the east. These $S-P$ conversions probably occur well away from the subducting slab, whereas our raypaths from the North section travel almost parallel to the Tonga slab.

The study by Bock & Ha (1984) included mostly events from the South section of Tonga. Their apparent conversion depths are quite scattered (Fig. 6), clustering around 700 km. Our nonlinear stack section for the South section (Fig. 11c) also shows this scatter of coherent arrivals in the $S_{670}P$ time window. We tentatively call this a double arrival.

The first pulse is more well-defined and is the only clear candidate for $S_{670}P$. The combination of a larger data set and our data processing methods give better definition to this phase.

The later arrivals remain a mystery, and at present we can only speculate as to their origin. Plausible causes include $S-P$ conversion from a second discontinuity about 40 km deeper than the 670 km discontinuity, multipathing of rays travelling within and outside of the subducted slab, shear-wave splitting, and conversions from flat-lying 'dead' slabs in the transition zone. Top-side reflections from seismic structures below the subduction zone can be ruled out on the basis of simple raypath considerations (Ken Creager, personal communication).

Further insight is gained by subdividing the South section. Figs 16(a) and (b) show nonlinear stack sections for the northern (23.0–24.2 S lat.) and southern (24.2–26.0 S lat.) parts of the South section. Arrivals in the $S_{670}P$ window of

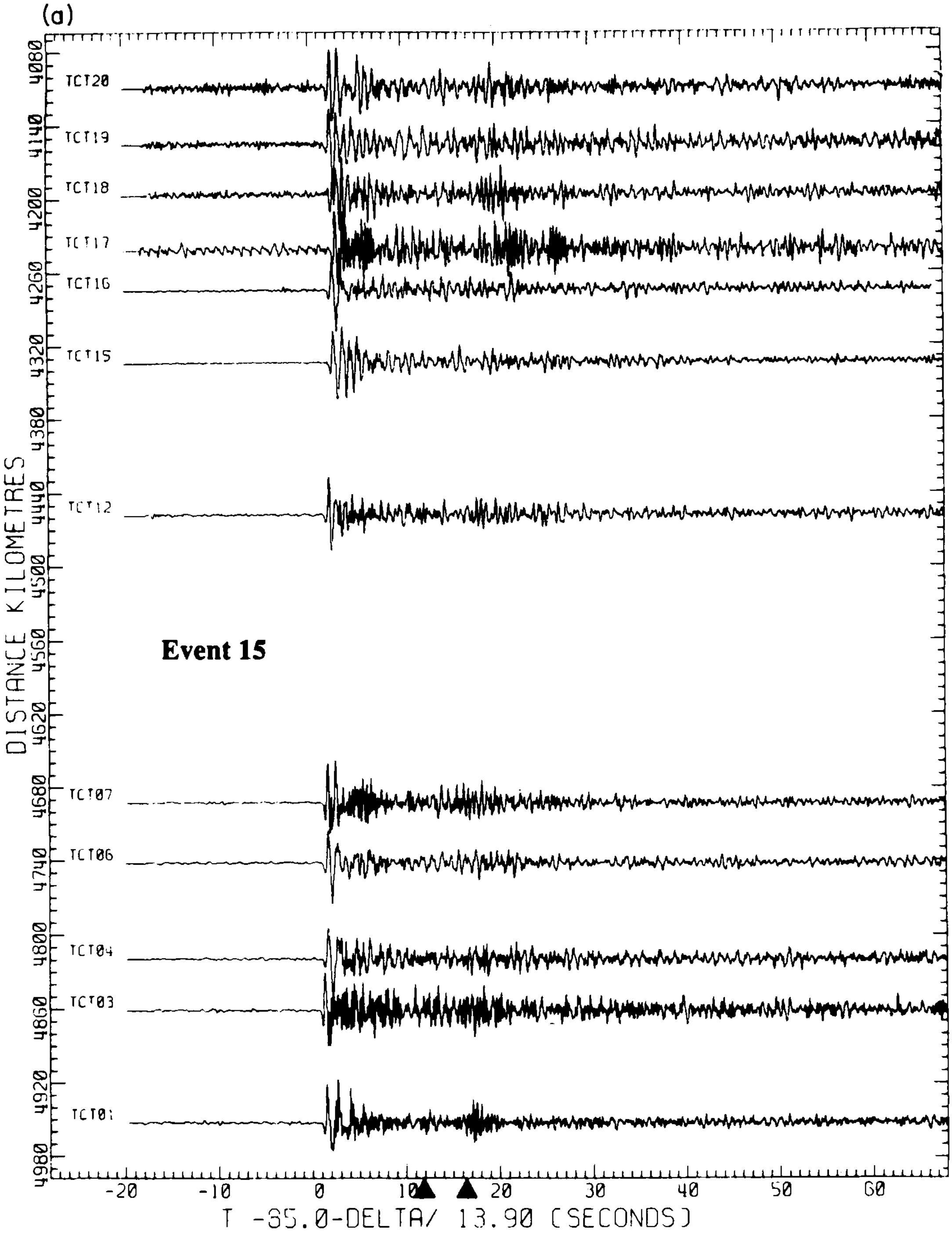

Figure 15. (a) Short-period recordings from the TCT array (see Fig. 1) for event 15 from Table 1. The applied travel time reduction is on the time axis label. Coda arrivals at about 12 and 16 s after *P* which were found on the WRA stacks are indicated by arrowheads on the time axis. No filtering has been applied. (b) Same as Fig. 15(a), except for event 16 from Table 1.

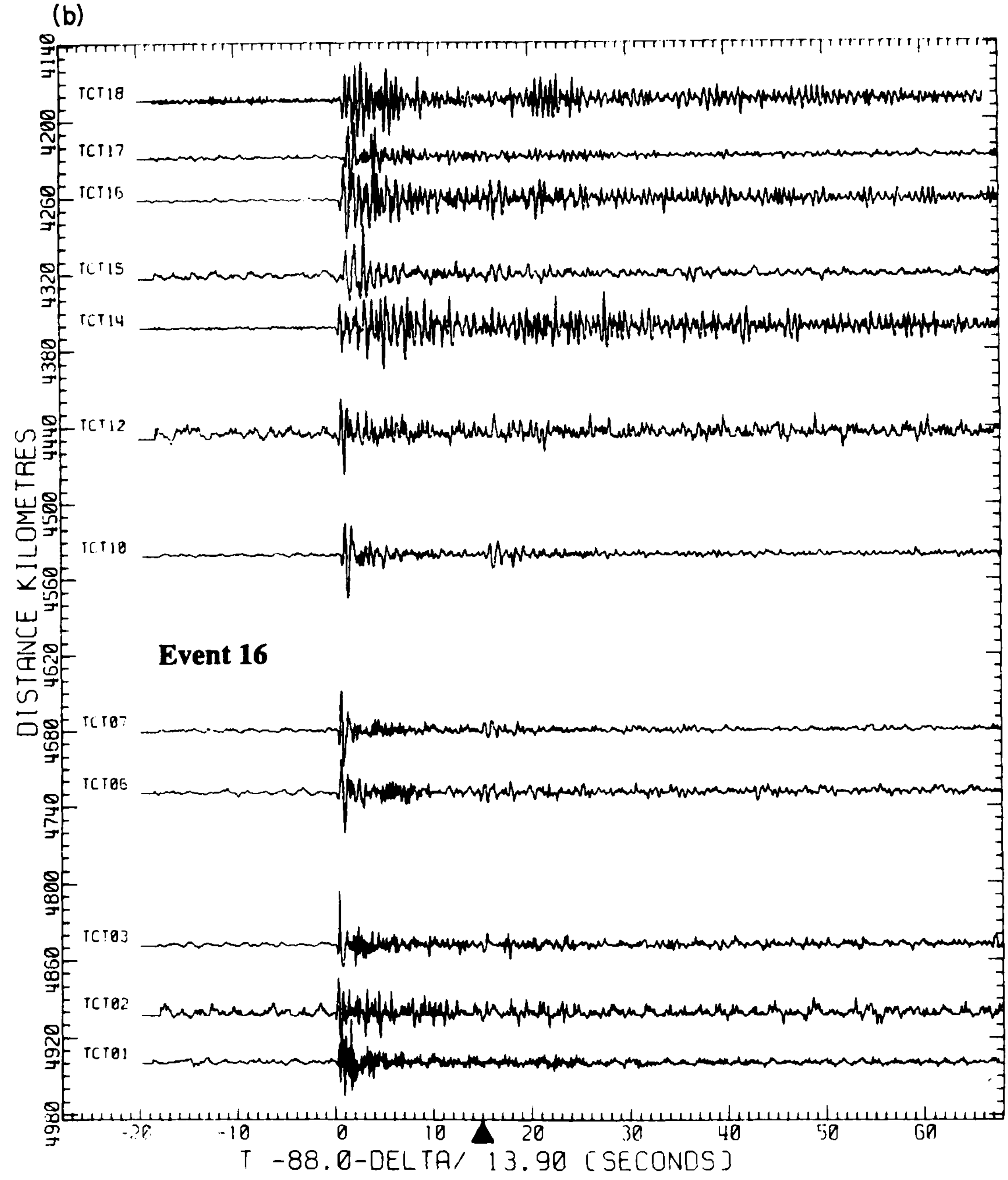

Figure 15. (*continued*)

the northern part (Fig. 16a) are rather complicated, and it would be difficult to isolate the phase from this section alone. The southern part (Fig. 16b) yields a much more consistent $S_{670}P$ arrival (apparent conversion depth ~660 km). Also, a second arrival appears about 5 s after $S_{670}P$ on at least five of the stack traces.

These two subsections are quite different in profile. As shown by Giardini & Woodhouse (1984), the slab apparently has two deep lobes side-by-side just above 670 km in the northern part (~23.0°S lat.). By contrast, the southern part (~25.0°S lat.) is much simpler in cross-section. It is difficult to say just how this difference in slab geometry might affect the occurrence of $S_{670}P$—slab heterogeneity effects, distortion of the 670 km discontinuity, and systematic source radiation pattern effects are possible causes. However, it is clear that by isolating the southern part of the South section, we find an $S-P$ conversion almost as prominent as that found in the North section.

5.2 Uncertainties in focal depths

Interpretation of our results depends strongly upon the accuracy of focal depth determinations. Systematic focal depth errors will obviously bias estimates for $S-P$ conversion depth. Fortunately, the ISC locations are generally quite accurate, largely because the station at Fiji

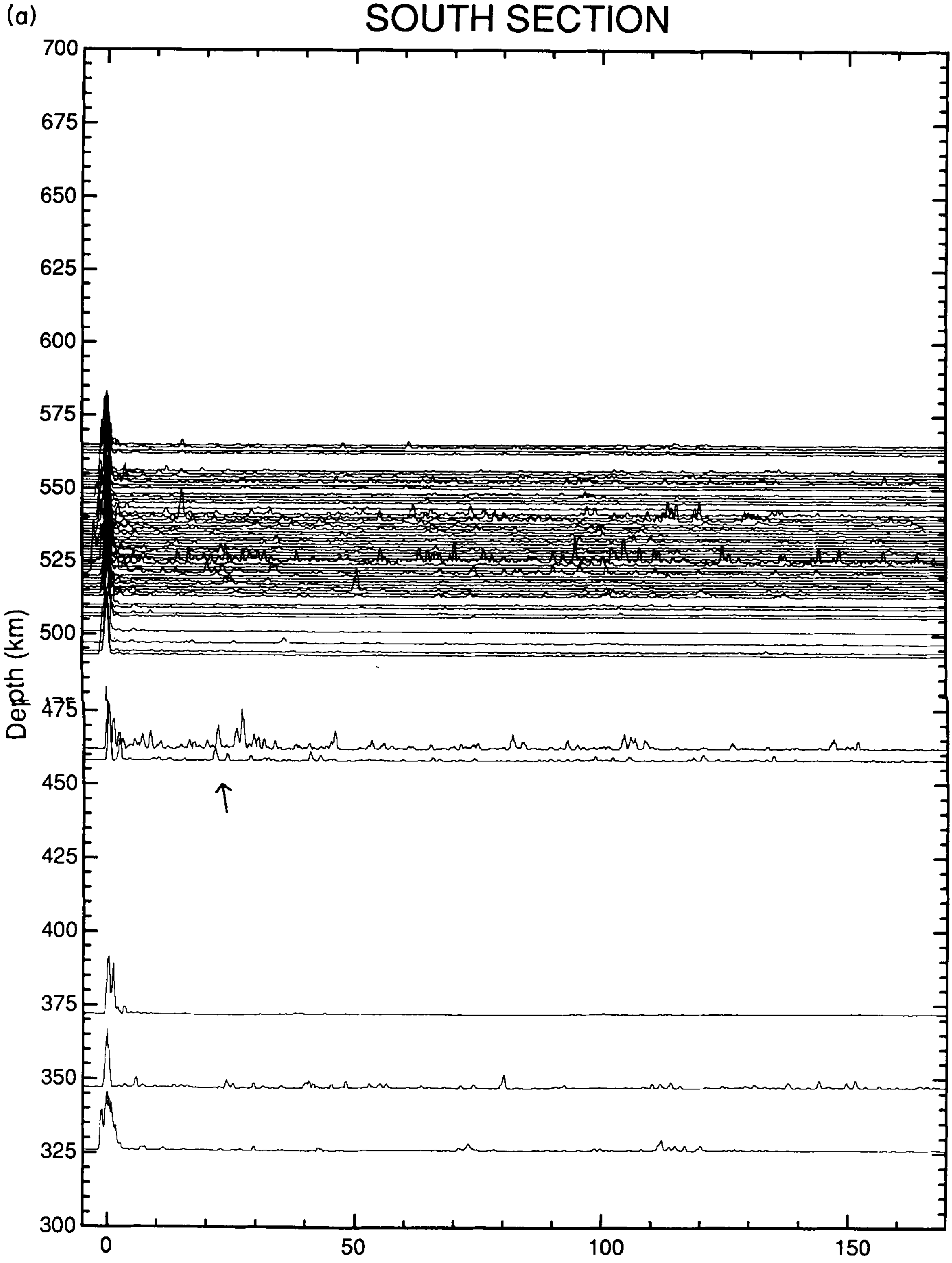

Figure 16. (a) Nonlinear stack section for the northern part of South Tonga (23.0°–24.2°S latitude). (b) Nonlinear stack section for the southern part of South Tonga (24.2–26.0°S latitude).

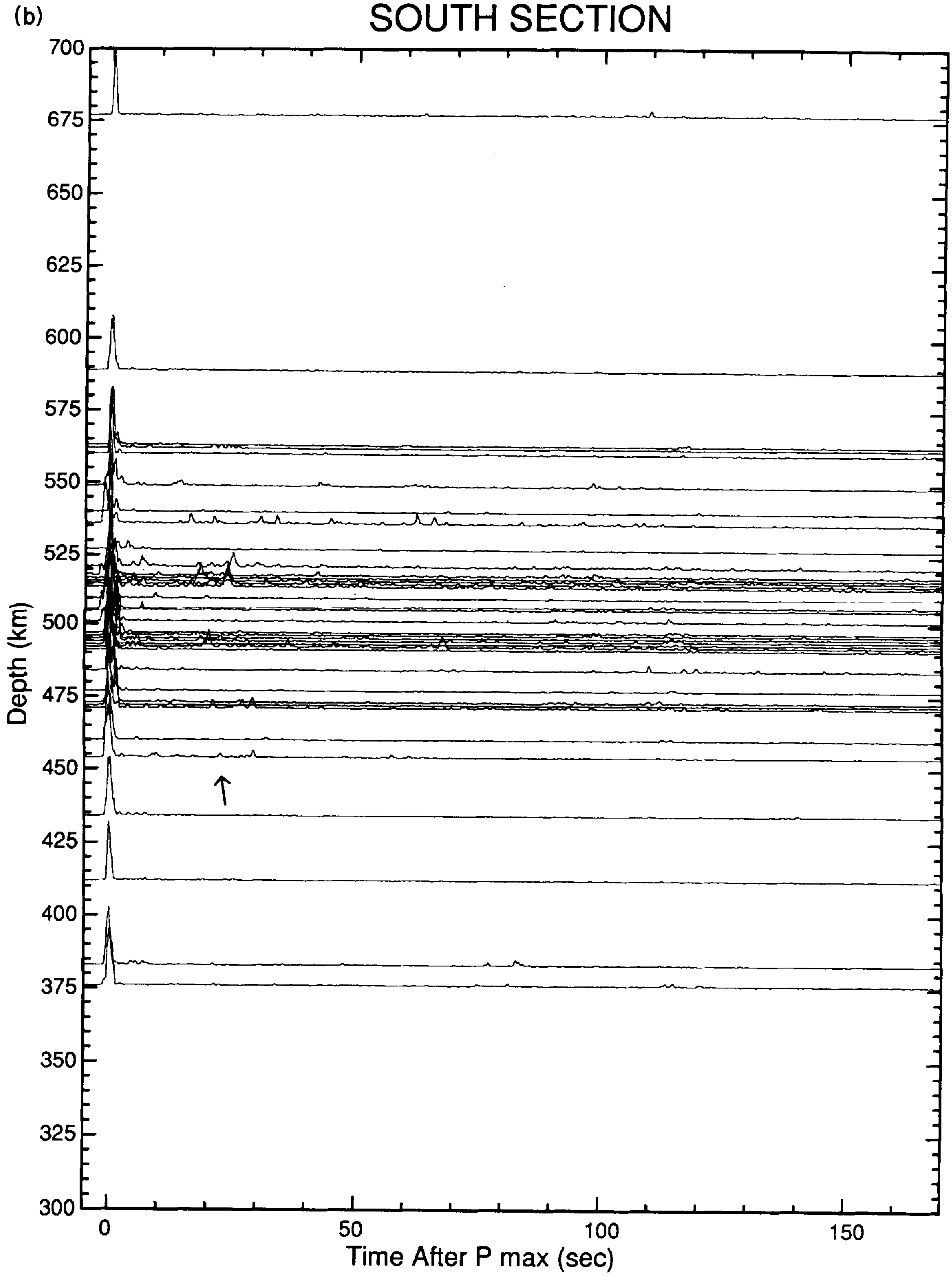

Figure 16. (*continued*)

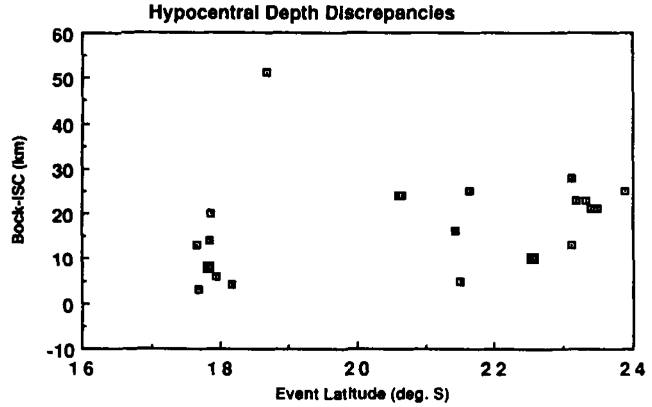

Figure 17. Plot of differences between the focal depth determinations of Bock (1987) and the ISC as a function of latitude along the Tonga subduction zone.

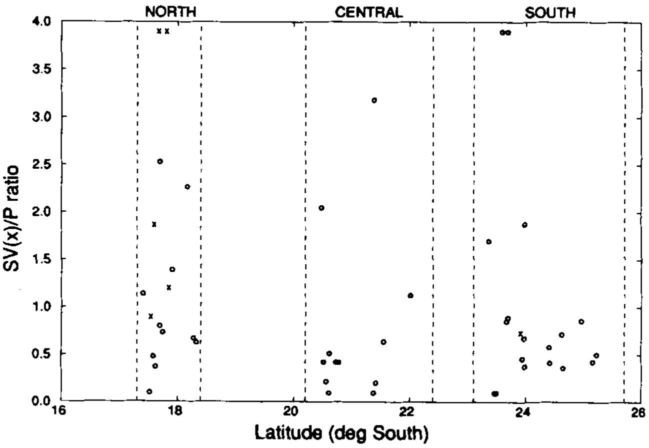

Figure 18. Calculated ratios of expected $S_{670}P$ to P amplitude ratios from Harvard CMT solutions for events with hypocentral depths <575 km. Amplitude ratios are for the SV and P legs above the 670 km discontinuity. Amplitude ratios greater than 4.0 have been clipped, because they represent near-nodal P-waves and are probably not very accurate.

provides good depth control (especially for the North section). Bock & Ha (1984) found only a small systematic difference between ISC determinations and focal depths determined from pP–P and ScP–PcP times: ISC hypocentres were about 5–10 km shallower.

Bock (1987) has recently completed a detailed study of seismic structure beneath North Tonga, using temporary seismic stations in the Tonga Islands. He simultaneously determined the effect of the slab on local travel times while estimating focal depths for deep earthquakes beneath Tonga using pP data. Most of the events Bock used are included in our data set. In Fig. 17 we compare ISC focal depths with Bock by plotting the difference (Bock–ISC) *vs.* latitude along the Tonga subduction zone. Except for one poorly located event, Bock's estimates are on average about 5–15 km deeper than ISC (similar to the small bias found by Bock & Ha 1984). Because Bock's study accounts for faster travel times along the fast slab to the island stations, we take his determinations to be more accurate. However, the main point is that the ISC locations appear by and large to be quite accurate. If the ISC locations are systematically about 10 km too shallow, this merely increases our estimate of S–P conversion depth by a similar amount.

5.3 Effects of radiation pattern

It is not surprising that $S_{670}P$ occurs with widely varying amplitude relative to P. The source radiation pattern will determine the relative amounts of P and SV energy directed along the raypaths toward WRA. Different focal mechanisms will produce different observed $S_{670}P/P$ ratios. Focal mechanisms for 79 of the events used in this study have been determined by the Harvard group (Dziewonski *et al.* 1982, 1983, 1984a,b, 1985a–d, 1986a,b, 1987a–c; Giardini 1984). We have used these moment tensor solutions in order to see if there is a systematic relationship between the occurrence of large $S_{670}P$ phases and favourable source mechanisms.

Figure 18 shows calculated SV/P ratios for rays along the expected $S_{670}P$ and P raypaths. We have plotted only events with hypocentral depths less than 575 km, since $S_{670}P$ is not clearly observed for deeper events. Ratios are calculated for full moment tensor representations with a program written by Kennett (1988) using expressions from Aki & Richards (1980). The ratios are plotted versus latitude along the Tonga subduction zone, and ratios for events that exhibit particularly strong $S_{670}P$-phases are shown by ×s. As we might have expected from the $S_{670}P$ results above, the largest SV/P ratios (on average) are found in the North section and the smallest in the Central section. Also, all of the five '×' events in the North show large calculated SV/P ratios. [We note that these results are somewhat different than the SV/P ratios that Bock & Ha (1984) calculated from Billington's (1980) focal mechanism solutions, because we have included only events less than 575 km in hypocentral depth. Since neither Barley *et al.* (1982), Bock & Ha (1984), nor the present study have detected $S_{670}P$ for deeper events and since $S_{670}P$ is likely to be obscured by the P-wave arrival for events at greater depth, Fig. 18 clearly represents the hypocentral depth range of greatest interest.]

We have also observed strong ScP-phases (as well as PP) at Warramunga for events with strong $S_{670}P$ phases. Since the takeoff angles for ScP and $S_{670}P$ differ by only about 12°, this supports the idea that systematic variations in short-period SV radiation patterns are responsible for the variability in $S_{670}P$ observations along the Tonga subduction zone. Moreover, the deep seismicity patterns of the Tonga slab suggest to us that these variations in SV radiation result from variations in dominant fault plane orientations in the deep slab. In both the South and Central sections, the deep seismicity is dominated by events along a gently north-dipping 'megashear' zone identified by Giardini & Woodhouse (1984, 1986). This results in focal mechanisms that are generally unfavorable for SV radiation toward WRA. The megashear extends throughout the Central section and into the northern part of the South section (refer to Fig. 4), and these are just the sections where we do not observe $S_{670}P$ (Figs 11b and 16b). By contrast, seismicity patterns in the North section indicate that rupture planes dip downward or along the subducting slab (Giardini & Woodhouse 1984, 1986). These focal mechanisms are more favorable for SV radiation (S–P conversion) in the direction of WRA.

Two other radiation pattern effects may also be present. First, strong lateral heterogeneity near the slab will cause focussing and defocussing and distort the radiation pattern. Second, for short-period waves the fault rupture propagation or directivity effect may be important even for small ($m_b \sim 5.0$) events. In fact, comparison of observed and calculated SV/P ratios suggests some enhancement of $S_{670}P$ in the North section due to source directivity. We will discuss this issue in detail, along with the moment tensor and ScP results mentioned above, in a future paper concentrating on radiation pattern effects in the North section (Wicks & Richards, unpublished manuscript). For the present purpose, we conclude simply that all observational evidence indicates that SV radiation toward WRA is strongest when $S_{670}P$ is observed, regardless of the cause. This supports the interpretation of the phase as an S–P conversion beneath the source.

5.4 Slab geometry, lateral heterogeneity, and raypaths

Some problems arise in interpreting $S_{670}P$ travel times because of large expected seismic heterogeneities in the subduction zone. Both along-path velocity variations and raypath distortion could give apparent $S_{670}P$ conversion depths different from the true depth of the discontinuity. Some simple calculations illustrate possible effects of velocity heterogeneity. Consider an earthquake at 550 km depth, for which the observed $S_{670}P$–P delay in the North section is about 13.5 s. Now suppose that the true discontinuity is at 690 km instead of the apparent depth of 670 km, and that the discrepancy is entirely a consequence of an anomalously fast S-wave velocity between the source and the discontinuity. The true S-leg travel path is only about 180 km long. For a reference S-wave velocity of $5.3\,\mathrm{km\,s^{-1}}$ and a reference P-wave velocity of $10.0\,\mathrm{km\,s^{-1}}$, the anomalous S-wave velocity must be about $5.8\,\mathrm{km\,s^{-1}}$ to give an apparent conversion depth of only 670 km (13.5 s delay). This represents an S-wave velocity contrast of almost 10 per cent. The P-waves are almost equally as likely to travel within the high velocity slab. If the P-wave velocity along the P travel path increases also, then the S-wave contrast must be even larger to account for the travel time difference since both P and $S_{670}P$ will be advanced.

We will not debate here whether or not such large S-velocity contrasts may exist—they probably do within the slab. However, the main point is that even for large velocity contrasts for either P- or S-waves, the true depth of conversion is probably not more than several tens of kilometres different from the apparent conversion depth. Considering also uncertainties in hypocentral depth control, we conclude that our apparent conversion depths are unlikely to be more than about 10–30 km too shallow.

This conclusion becomes more important when we consider the $S_{670}P$ raypaths from Tonga to WRA. The slab geometry below about 400 km is complicated (see Fig. 2 of Giardini & Woodhouse 1984). In North Tonga the slab-dip, insofar as it can be defined, is between about 60° and near-vertical. In Central Tonga the dip is about 60–70°. In South Tonga the slab geometry ranges from about 60° dip in the far south (where $S_{670}P$ is most clearly observed) to a complicated bench-like, double-lobed structure to the north. In all cases, $S_{670}P$ (takeoff angle 25°, or 65° 'dip') travels subparallel to the slab. The slab is faster than surrounding mantle (e.g., Bock 1981, 1987), due perhaps to phase changes (Ringwood 1982; Anderson 1987) as well as colder temperatures, and will act as an 'anti-lens', tending to diffuse seismic energy. As a result, rays that travel to WRA will, if anything, have even more tendency to start off travelling within and/or parallel to the slab to avoid being refracted away.

Preliminary calculations of raypaths and travel times in heterogeneous slab models (K. C. Creager, personal communication) demonstrate this effect for the Tonga–WRA source-receiver geometry. However, it is difficult to develop any definitive model for raypath distortion without much better *a priori* knowledge of seismic heterogeneity beneath Tonga than is currently available. The slab itself is highly contorted, especially beneath North Tonga, and its depth of penetration into the lower mantle is quite controversial. For the present purpose, the most noteworthy effect of the high-velocity slab will be to draw both the P and S–P raypaths more nearly parallel to the slab. This will result in takeoff angles only ~5–10° different from those predicted by a simple radial earth model, and any travel time anomalies will result primarily from along-path velocity anomalies.

If we assume that most of the deep earthquakes occur near the coldest part or core of the slab, then the S–P conversions observed must be taking place either within or immediately adjacent to the subducted slab. Even unperturbed S–P raypaths (Fig. 3) will most likely encounter the 670 km discontinuity within the slab. In the North section in particular, the 'hook' geometry of the downgoing slab is such that the strike of the slab is more nearly parallel than perpendicular to the WRA–Tonga raypath (Figs 4 and 5). Therefore, in the section from which we have the most reliable observations of $S_{670}P$, the S–P conversions are even more likely to occur within the steeply dipping slab. This has important implications: First, it is remarkable that the $S_{670}P$ phase exists at all under such conditions. If either the thermal anomaly of the slab or slightly different slab mineralogy leads to elevation or depression of the discontinuity, distortion of the otherwise 'flat' discontinuity surface near and within the slab would defocus or scatter the converted waves. Secondly, and more importantly, the simplest interpretation is that the 670 km discontinuity occurs at essentially the same depth within the slab as in the surrounding 'normal' mantle. That is, of course, dynamically implausible if the discontinuity results from a chemical boundary layer. Reasoning that the 670 km discontinuity below Tonga is instead an abrupt phase change, we conclude that it must be almost entirely pressure-dependent.

A great deal more fine tuning is desirable, and 3-D tracing through slab models for Tonga may allow us to place better bounds on the effects of lateral heterogeneity near the slab. However, based on preliminary calculations and some straightforward reasoning, we do not believe that major modifications to our interpretation will result. One additional avenue for further work will be a detailed comparison of P and $S_{670}P$ waveforms. The largest $S_{670}P$ arrivals so far examined from linear stacks (which preserve waveforms) appear similar to the P-waves at ~1 s period. So far, we see no evidence for waveform distortion upon conversion at the 670 km discontinuity, consistent with a simple, sharp phase boundary.

6 CONCLUSIONS

The main purpose of this study was to demonstrate whether or not the $S-P$ converted phase $S_{670}P$ was clearly observable for deep earthquakes beneath the Tonga subduction zone. For the North and South sections defined here, we found strong $S_{670}P$ phases in the P-wave codas recorded at the Warramunga Seismic Array in central Australia. A very large data set was examined, including more than 300 events of magnitude $m_b \geq 4.8$. The best results were obtained by using nonlinear (nth root) stacks of the 20 vertical channels from WRA, and by combining the stacks into focal depth sections that naturally show coherent P-coda phases at the selected stacking slowness. These sections (and slant-stacks through these sections) also show the correct focal depth *vs.* delay with respect to P for the phases identified as $S_{670}P$.

By dividing the subduction zone into three sections (North, Central, and South) which contain dense concentrations of deep earthquake hypocentres, we were able to examine some details of the geographical variability of $S_{670}P$. The clearest $S-P$ conversions were observed from the North section for events between 500 and 575 km focal depth. Here, the apparent $S-P$ conversion depth was about 660 to 690 km (corrected for about 10 km estimated systematic error in focal depth determinations from the ISC). For Central Tonga $S_{670}P$ is not clearly observed, probably because of unfavourable source radiation patterns. For the South section $S_{670}P$ is again observed (especially in the latitude range 24.2–26.0°S), and a second phase appears to follow $S_{670}P$ by about 5 s. (There is also a subtle hint of a similar second phase from the North section.) The apparent conversion depth for the first $S_{670}P$-phase is about 660 to 700 km (again corrected for estimated focal depth errors) for events between 450 and 550 km focal depth. Somewhat larger $S_{670}P-P$ delays for deeper events suggest that the 670 km discontinuity may be depressed by ~20–30 km within the subducting slab, although seismic velocity heterogeneities could also be responsible for these small delay anomalies. The origin of the second phase is unknown. If it is an $S-P$ conversion, the apparent conversion depth would be about 700 to 740 km, but this interpretation is probably premature.

If the simplest interpretation is accepted, our results imply little dynamical deformation or warping of the 670 km discontinuity. Given (1) that large deformations of a chemical boundary layer must occur beneath the downgoing Tonga slab, (2) that the $S-P$ converted waves we have observed must travel either very close to or within the slab, and (3) that the conversions occur at very short-period, we offer the following conclusion: the 670 km discontinuity beneath Tonga is the result of a phase transition which occurs over a very restricted depth interval (~5 km or less) and which may occur at similar depths within both the cold, subducting slab and the surrounding mantle. (Somewhat greater conversion depths for $S-P$ phases from deeper events could result from thermal depression of a moderately endothermic phase reaction.) This does not rule out a chemical boundary layer or gradient in the transition zone, but it does imply that the jump in seismic velocity observed worldwide at about 650 to 670 km results from a phase transition.

ACKNOWLEDGMENTS

This work was supported by a postodoctoral fellowship awarded to M.R. by the Australian National University and by National Science Foundation Grant EAR-8720965. We thank Brian Kennett for providing access to the WRA data and for providing the program to calculate radiation patterns. John Woodhouse and Domenico Giardini generously sent us the Harvard CMT solutions and relocated hypocentres from their previous work. Ken Creager provided much insight into raypath problems in subduction zones. Don Anderson originally suggested this area of research to M.R. We thank Michael Korn and Doug Christy for help in extracting the WRA data from archive tapes. Careful reviews by Gunter Bock and an anonymous reviewer improved the manuscript. Discussions with Anton Hales were also helpful.

REFERENCES

Aki, K. & Richards, P. G., 1980. *Quantitative Seismology: Theory and Methods*, W. H. Freeman, San Francisco.

Anderson, D. L., 1987. Thermally induced phase changes, lateral heterogeneity of the mantle, continental roots, and deep slab anomalies, *J. geophys. Res.*, **92,** 13 968–13 980.

Barley, B. J., 1977. The origin of complexity in some P seismograms from deep earthquakes, *Geophys. J. R. astr. Soc.*, **49,** 773–777.

Barley, B. J., Hudson, J. A. & Douglas, A., 1982. S to P scattering at the 650 km discontinuity, *Geophys. J. R. astr. Soc.*, **69,** 159–172.

Billington, S., 1980. The morphology and tectonics of the subducted lithosphere in the Tonga–Fiji–Kermadec region from seismicity and focal mechanism solutions, *PhD thesis*, Cornell University, Ithaca, New York.

Bock, G., 1981. The effect of the descending lithosphere beneath the Tonga island arc on P-wave travel-time residuals at the Warramunga Seismic Array, *Phys. Earth planet. Inter.*, **25,** 360–371.

Bock, G., 1987. P-wave travel times from deep and intermediate-depth earthquakes to local seismic stations and the subducted slab of oceanic lithosphere beneath the Tonga island arc, *J. geophys. Res.*, **92,** 13 863–13 877.

Bock, G. & Ha, J., 1984. Short-period $S-P$ conversion in the mantle at a depth near 700 km, *Geophys. J. R. astr. Soc.*, **77,** 593–615.

Christensen, U. R. & Yuen, D. A., 1984. The interaction of a subducting lithospheric slab with a chemical or phase boundary, *J. geophys. Res.*, **89,** 4389–4402.

Cleary, J., 1981. Seismic wave scattering on underside reflection at the core–mantle boundary, *Phys. Earth planet. Inter.*, **26,** 266–267.

Dziewonski, A. M. & Woodhouse, J. H., 1982. An experiment in the systematic study Centroid-moment tensor solutions for October–December 1985, *Phys. Earth planet. Inter.*, **43,** 185–195.

Dziewonski, A. M., Franzen, J. E. & Woodhouse, J. H., 1984a. Centroid-moment tensor solutions for April–June 1983, *Phys. Earth planet. Inter.*, **34,** 1–8.

Dziewonski, A. M., Franzen, J. E. & Woodhouse, J. H., 1984b. Centroid-moment tensor solutions for January–March 1984, *Phys. Earth planet. Inter.*, **34,** 209–219.

Dziewonski, A. M., Franzen, J. E. & Woodhouse, J. H., 1985a. Centroid-moment tensor solutions for April–June 1984, *Phys. Earth planet. Inter.*, **37,** 87–96.

Dziewonski, A. M., Franzen, J. E. & Woodhouse, J. H., 1985b. Centroid-moment tensor solutions for July–September 1984, *Phys. Earth planet. Inter.*, **38,** 203–213.

Dziewonski, A. M., Franzen, J. E. & Woodhouse, J. H., 1985c. Centroid-moment tensor solutions for October–December 1984, *Phys. Earth planet. Inter.*, **39,** 147–156.

Dziewonski, A. M., Franzen, J. E. & Woodhouse, J. H., 1985d. Centroid-moment tensor solutions for January–March 1985, *Phys. Earth planet. Inter.*, **40,** 249–258.

Dziewonski, A. M., Franzen, J. E. & Woodhouse, J. H., 1986b. Centroid-moment tensor solutions for April–June 1985. *Phys. Earth planet. Inter.*, **41,** 215–224.

Dziewonski, A. M., Franzen, J. E. & Woodhouse, J. H., 1986c. Centroid-moment tensor solutions for July–September 1985, *Phys. Earth planet. Inter.*, **42,** 205–214.

Dziewonski, A. M., Ekström, G., Franzen, J. E. & Woodhouse, J. H., 1987a. Centroid-moment tensor solutions for January–March 1986, *Phys. Earth planet. Inter.*, **45,** 1–10.

Dziewonski, A. M., Ekström, G., Franzen, J. E. & Woodhouse, J. H., 1987b. Centroid-moment tensor solutions for April–June 1986, *Phys. Earth planet. Inter.*, **45,** 229–239.

Dziewonski, A. M., Franzen, J. E. & Woodhouse, J. H., 1987c. Centroid-moment tensor solutions for July–September 1986, *Phys. Earth planet. Inter.*, **46,** 305–315.

Dziewonski, A. M., Friedman, A., Giardini, D. & Woodhouse, J. H., 1983. Global seismicity of 1982: Centroid-moment tensor solutions for 308 earthquakes, *Phys. Earth planet. Inter.*, **33,** 76–90.

Dziewonski, A. M., Hales, A. L., & Lapwood, E. R., 1975. Parametrically simple earth models consistent with geophysical data, *Phys. Earth planet. Inter.*, **10,** 12.

Engdahl, E. R. & Flinn, E. A., 1969. Seismic waves reflected from discontinuities within Earth's upper mantle, *Science,* **163,** 177–179.

Faber, S. & Muller, G., 1984. Converted phases from the mantle transition zone at European stations, *J. geophys. Res.*, **54,** 183–194.

Giardini, D., 1984. Systematic analysis of deep seismicity: 200 centroid–moment tensor solutions for earthquakes between 1977 and 1980, *Geophys. J. R. astr. Soc.*, **77,** 883–914.

Giardini, D. & Woodhouse, J. H., 1984. Deep seismicity and modes of deformation in Tonga subduction zone, *Nature,* **307,** 505–509.

Giardini, D. & Woodhouse, J. H., 1986. Horizontal shear flow in the mantle beneath the Tonga arc, *Nature,* **319,** 551–555.

Grand, S. P. & Helmberger, D. V., 1984. Upper mantle shear structure beneath the northwest Atlantic Ocean, *J. geophys. Res.*, **89,** 11 465–11 475.

Hager, B. H. & Raefsky, A., 1981. Deformation of seismic discontinuities and the scale of mantle convection, *EOS, Trans. Am. geophys. Un.*, **62,** 1074.

Jeanloz, R. & Thompson, A. B., 1983. Phase transitions and mantle discontinuities, *Rev. Geophys. Space Phys.*, **21,** 51–74.

Kanasewich, E. R., Hemmings, C. D. & Alpaslan, I., 1973. *N*th-root stack non-linear multichannel filter, *Geophysics,* **38,** 327–328.

Kennett, B. L. N., 1988. Radiation from a Moment-Tensor Source, in *Seismological Algorithms,* pp. 427–441, Academic Press, Princeton, NJ.

Kincaid, C. & Olson, P., 1987. An experimental study of subduction and slab migration, *J. geophys. Res.*, **92,** 13 832–13 840.

Muirhead, K., 1968. Eliminating false alarms when detecting seismic events automatically, *Nature,* **217,** 533–534.

Muirhead, K., 1985. Comments on "Reflection properties of phase transition and compositional change models of the 670-km discontinuity" by Alison C. Lees, M. S. T. Bukowinski, and Raymond Jeanloz, *J. geophys. Res.*, **90,** 2057–2059.

Muirhead, K. J. & Datt, F., 1976. The *N*-th root process applied to seismic array data, *Geophys. J. R. astr. Soc.*, **47,** 197–210.

Nakanishi, I., 1986. Seismic reflections from the upper mantle discontinuities beneath the mid-Atlantic ridge observed by a seismic array in Hokkaido region, Japan, *Geophys. Res. Lett.*, **13,** 1458–1461.

Paulssen, H., 1985. Upper mantle converted waves beneath the NARS array, *Geophys. Res. Lett.*, **12,** 709–712.

Paulssen, H., 1987. Evidence for a sharp 670-km discontinuity from *P* to *S* converted waves, abstract, *EOS, Trans. Am. geophys. Un.*, **68,** 1379.

Richards, P. G., 1972. Seismic waves reflected from velocity gradient anomalies within the Earth's upper mantle, *Z. Geophys.*, **38,** 517.

Ringwood, A. E., 1982. Phase transformations and differentiation in subducting lithosphere: Implications for mantle dynamics, basalt petrogenesis, and crustal evolution, *J. Geol.*, **90,** 611–643.

Takahashi, E. & Ito, E., 1988. Constitution and chemical evolution of the Earth's mantle: Implications from high pressure experiments, *First SEDI Symposium,* Blanes, Spain.

Whitcomb, J. H. & Anderson, D. L., 1970. Reflection of *P'P'* seismic waves from discontinuities in the mantle, *J. geophys. Res.*, **75,** 5713–5728.